

submitted to *Geophys. J. Int.*

Magnetic radial inversion for 3-D source geometry estimation

L.B. Vital^{1*}, V.C. Oliveira Jr.¹ and V.C.F. Barbosa¹

¹ *Observatório Nacional, Gal. José Cristino, 77, São Cristóvão, Rio de Janeiro, 20921-400, Brazil*

SUMMARY

We present a method for inverting total-field anomaly data to estimate the geometry of a uniformly magnetized 3-D geological source in the subsurface. The method assumes the total-magnetization direction is known. We approximate the source by an ensemble of vertically juxtaposed right prisms, all of them with the same total-magnetization vector and depth extent. The horizontal cross-section of each prism is a polygon defined by a given number of equi-angularly spaced vertices from 0° to 360° , whose polygon vertices are described by polar coordinates with an origin defined by a horizontal location over the top of each prism. Because our method estimates the radii of each polygon vertex we refer to it as *radial inversion*. The position of these vertices, the horizontal location of each prism, and the depth extent of all prisms are the parameters to be estimated by solving a constrained nonlinear inverse problem of minimizing a goal function. We run successive inversions for a range of tentative total-magnetization intensities and depths to the top of the shallowest prism. The estimated models producing the lowest values of the goal function form the set of candidate solutions. To obtain stabilized solutions, we impose the zeroth- and first-order Tikhonov regularizations on the shape of the prisms. The method allows estimating the geometry of both vertical and inclined sources, with a constant direction of magnetization, by using the Tikhonov regularization. Tests with synthetic data show that the method can be of utility in estimating the shape of the magnetic source even in the presence of a strong regional field. Results obtained by inverting airborne total-field anomaly data over the Anitápolis alkaline-carbonatitic complex, in southern Brazil, suggest that the emplacement of the magnetic sources was controlled by NW-SE-trending faults at depth, in accordance with known structural features at the study area.

Key words: Magnetic anomalies: modeling and interpretation; Inverse theory; Numerical solutions.

1 INTRODUCTION

The interpretation of total-field anomalies on the surface of the Earth is an important challenge in exploration geophysics due to the nonuniqueness of 3-D magnetic inversion. It is well-known that several magnetization distributions in the subsurface can reproduce the same magnetic data with the same accuracy. To overcome this inherent ambiguity, a priori information needs to be introduced for reducing the number of possible solutions that are coherent with the local geology. The available a priori information determines the suitable inversion method to be applied. As explained below, we identified, in the literature, three groups of 3-D magnetic inversion methods.

The first group of inverse methods approximates the source by a geometrically simple causative body having its geometry defined by a small number of parameters (e.g., Ballantyne 1980; Bhattacharyya 1980; Silva & Hohmann 1983; Medeiros & Silva 1995). These methods estimate both the geometry and the physical property of the source by solving a nonlinear inverse problem. Due to the very restrictive parametrization, such methods usually do not have severe problems with ambiguity.

The second group of inverse methods is formed by the vast majority of methods. These methods approximate the subsurface by a grid of juxtaposed rectangular prisms having a constant total-magnetization direction. Some methods presume a purely induced magnetization and the isotropic magnetic susceptibility of the prisms is the quantity estimated by solving a linear inverse problem. Some examples of this linear inversion are presented by Cribb (1976), Li & Oldenburg (1996) and Pilkington (1997). Different approaches have improved this linear inversion to obtain focused images of the subsurface. For example, Portniaguine & Zhdanov (1999) and Portniaguine & Zhdanov (2002) introduced the minimum gradient support functional, similar to the one proposed by Last & Kubik (1983) that minimizes the volumes of the sources in a gravity data inversion. By inverting magnetic anomaly and any component of the total anomalous field, this functional estimates a magnetization distribution that generates a non blurry (focused) 3-D image of the geologic bodies in the subsurface. Barbosa & Silva (2006) presented a method for inverting interfering magnetic anomalies produced by multiple sources by combining features of the forward modeling (the interactivity) and traditional inversion (the automatic data fitting). Other studies introduced strategies to constraint the nonuniqueness and delineate the source (Caratori Tontini et al. 2006; Pilkington 2009; Shamsipour et al. 2011; Cella & Fedi 2012; Abedi et al. 2015). Some of these methods allowed remanent magnetization (e.g., Pignatelli et al. 2006). In this case, the parameters to be estimated are the total-magnetization intensities of the prisms. In all these methods, the geometries of the magnetic sources are indirectly retrieved by interpreting the estimated total-magnetization intensity distribution. Theoretically, these inversion methods are capable of recovering the geometry of complex sources. However, they require a plethora of a priori information to overcome their nonuniqueness and instability due to the large number of pa-

rameters to be estimated. Additionally, they are characterized by a high computational cost associated with the solution of large linear systems.

The third group of 3-D magnetic inversion methods requires some knowledge about the physical property distribution to estimate the geometry of the sources. They are usually formulated as nonlinear inverse problems. Wang & Hansen (1990) approximated the source by a polyhedron and estimate the position of its vertices in the Fourier domain. Li et al. (2017) developed a multiple level-set method to estimate geometry of a set of causative bodies with uniform magnetic susceptibility. Hidalgo-Gato & Barbosa (2019) inverted the total-field anomaly for estimating the depths to the top of a magnetic basement of a sedimentary basin with known magnetization intensity but unknown magnetization direction. An inverse method in this third group has a small number of parameters to be estimated by inversion and has much less ambiguity in comparison to the second group.

By following the third group of 3-D magnetic inversion methods, we present a method to estimate the geometry, position and total-magnetization intensity of an isolated and uniformly magnetized 3-D source with known total-magnetization direction. Our method is an extension of the methods presented by Oliveira Jr. et al. (2011) and Oliveira Jr. & Barbosa (2013) for inverting, respectively, gravity and gravity-gradient data, applied to the total-field anomaly. We approximate the source by a stack of vertically juxtaposed right prisms with polygonal horizontal cross-sections and the same number of vertices. All prisms have the same thickness and total-magnetization intensity. Differently from Oliveira Jr. et al. (2011) and Oliveira Jr. & Barbosa (2013), our method estimates not only the horizontal Cartesian coordinates of the origins and the radii of the vertices describing the horizontal cross-sections of all prisms but also the thickness of all prisms comprising the interpretation model, as well as two additional parameters: the depth to the top of the shallowest prism and the total-magnetization intensity of all prisms. We perform a series of inversion runs using different value combinations of these two parameters and compute a goal function associated with each of the trial solutions. Among the estimated models, those producing the lowest values of goal function form the set of candidate models. To obtain stable solutions, we use the same set of regularizing functions proposed by Oliveira Jr. et al. (2011) and also propose a new one for constraining the thickness of the prisms. Following Oliveira Jr. et al. (2011) and Oliveira Jr. & Barbosa (2013), we refer to the proposed method as *radial inversion* because our method estimates the radii of the vertices describing the horizontal cross-sections of all prisms. Tests on synthetic data and on airborne magnetic data collected over the alkaline-carbonatitic complex of Anitápolis, in southern Brazil, show the potential of our method in retrieving 3-D magnetic bodies even if they exhibit a variety of shapes and depths.

2 METHODOLOGY

2.1 Forward problem

Let \mathbf{d}^o be the observed data vector, whose i th element d_i^o , $i = 1, \dots, N$, is the total-field anomaly produced by a 3-D source (Fig. 1a) at the point (x_i, y_i, z_i) of a Cartesian coordinate system with x -, y - and z - axes pointing to north, east and down, respectively. We assume that the direction of the total magnetization vector of the source is constant and known. We approximate the volume of the source by a set of L vertically juxtaposed 3-D prisms (Fig. 1b) by following the same approach of Oliveira Jr. et al. (2011) and Oliveira Jr. & Barbosa (2013). The depth to the top of the shallowest prism is defined by z_0 , and m_0 is the constant total-magnetization intensity of all prisms. The horizontal cross-section of each prism (Fig. 2) is described by a polygon with a fixed number V of vertices equi-angularly spaced from 0° to 360° , which are described in polar coordinates referred to an internal origin O^k . The radii of the vertices (r_j^k , $j = 1, \dots, V$, $k = 1, \dots, L$), the horizontal coordinates (x_0^k and y_0^k , $k = 1, \dots, L$) of the origins O^k , $k = 1, \dots, L$, and the thickness dz of the L vertically stacked prisms (Fig. 1b) are arranged in a $M \times 1$ parameter vector \mathbf{p} , $M = L(V + 2) + 1$, given by

$$\mathbf{p} = \begin{bmatrix} \mathbf{r}^{1\top} & x_0^1 & y_0^1 & \dots & \mathbf{r}^{L\top} & x_0^L & y_0^L & dz \end{bmatrix}^\top, \quad (1)$$

where “ \top ” denotes transposition and \mathbf{r}^k is a $V \times 1$ vector containing the radii r_j^k of the k th prism. Let $\mathbf{d}(\mathbf{p}, m_0, z_0)$ be the predicted data vector, whose i th element

$$d_i(\mathbf{p}, m_0, z_0) \equiv m_0 \sum_{k=1}^L f_i(\mathbf{r}^k, x_0^k, y_0^k, dz, z_0), \quad i = 1, \dots, N, \quad (2)$$

is the total-field anomaly produced by the ensemble of L prisms at the i th observation point (x_i, y_i, z_i) . In Eq. 2, $f_i(\mathbf{r}^k, x_0^k, y_0^k, dz, z_0)$ is the total-field anomaly produced, at the observation point (x_i, y_i, z_i) , by the k th prism with unitary magnetization intensity and depth to the top $z_1^k = z_0 + (k - 1)dz$. We calculate $d_i(\mathbf{p}, m_0, z_0)$ (Eq. 2) by using the Python package Fatiando a Terra (Uieda et al. 2013), which implements the formulas proposed by Plouff (1976).

2.2 Inverse problem for estimating \mathbf{p}

Given the depth to the top of shallowest prism z_0 and the total-magnetization intensity m_0 of all prisms, we solve a constrained nonlinear problem to estimate the parameter vector \mathbf{p} (Eq. 1) by minimizing the goal function

$$\Gamma(\mathbf{p}, m_0, z_0) = \phi(\mathbf{p}, m_0, z_0) + \sum_{\ell=1}^7 \alpha_\ell \varphi_\ell(\mathbf{p}), \quad (3)$$

subject to the inequality constraints

$$p_l^{min} < p_l < p_l^{max}, \quad l = 1, \dots, M. \quad (4)$$

The first term in the right side of Eq. 3 is the data-misfit function given by

$$\phi(\mathbf{p}, m_0, z_0) = \frac{1}{N} \|\mathbf{d}^o - \mathbf{d}(\mathbf{p}, m_0, z_0)\|_2^2, \quad (5)$$

which represents the normalized squared Euclidean norm of the difference between the observed \mathbf{d}^o and predicted $\mathbf{d}(\mathbf{p}, m_0, z_0)$ data vector, whose i th element is the predicted data $d_i(\mathbf{p}, m_0, z_0)$ (Eq. 2). The second term in the right side of Eq. 3 represents the weighted sum of the seven constraint functions $\varphi_\ell(\mathbf{p})$, $\ell = 1, \dots, 7$, described in the following section *Constraint functions*. In Eq. 3, α_ℓ is a positive number representing the weight of the ℓ th constraint function $\varphi_\ell(\mathbf{p})$. In the inequality constraints (Eq. 4), p_l^{min} and p_l^{max} are, respectively, the lower and upper limits for the l th element p_l of the parameter vector \mathbf{p} (Eq. 1). These limits are defined by the interpreter based on the knowledge about the horizontal and total depth extensions of the magnetic source. Details about how we set the weights α_ℓ and the limits in the inequality constraints are presented in the section *Computational procedures* later in this article.

To solve our nonlinear inverse problem we use a gradient-based method and, consequently, we need to define an initial approximation $\hat{\mathbf{p}}_{(0)}$ for the parameter vector \mathbf{p} (Eq. 1). Then our method iteratively updates this initial approximation to obtain an estimated parameter vector $\hat{\mathbf{p}}_{(f)}$ minimizing the goal function $\Gamma(\mathbf{p}, m_0, z_0)$ (Eq. 3), for given values of total-magnetization intensity m_0 and depth to the top of the shallowest prism z_0 . Here, we use the superscript hat “ $\hat{\cdot}$ ” to denote initial approximation or estimated parameter vector.

Since we are using a gradient-based method, we need to define the gradient vector $\nabla\Gamma(\mathbf{p})$ and Hessian matrix $\mathbf{H}(\mathbf{p})$ of the goal function $\Gamma(\mathbf{p}, m_0, z_0)$ (Eq. 3), both of them computed with respect to the parameter vector \mathbf{p} . That is why we define them by omitting the parameters m_0 and z_0 . They are given by:

$$\nabla\Gamma(\mathbf{p}) = \nabla\phi(\mathbf{p}) + \sum_{\ell=1}^7 \alpha_\ell \nabla\varphi_\ell(\mathbf{p}) \quad (6)$$

and

$$\mathbf{H}(\mathbf{p}) = \mathbf{H}_\phi(\mathbf{p}) + \sum_{\ell=1}^7 \alpha_\ell \mathbf{H}_\ell, \quad (7)$$

where the gradient vector and the Hessian matrix of the misfit function $\phi(\mathbf{p})$ (Eq. 3) are respectively given by:

$$\nabla\phi(\mathbf{p}) = -\frac{2}{N} \mathbf{G}(\mathbf{p})^\top [\mathbf{d}^o - \mathbf{d}(\mathbf{p}, m_0, z_0)] \quad (8)$$

and

$$\mathbf{H}_\phi(\mathbf{p}) = \frac{2}{N} \mathbf{G}(\mathbf{p})^\top \mathbf{G}(\mathbf{p}). \quad (9)$$

In Eqs 6 and 7, the terms $\nabla \varphi_\ell(\mathbf{p})$ and \mathbf{H}_ℓ , $\ell = 1, \dots, 7$, are the gradient vectors and Hessian matrices of the constraint functions, respectively. In Eqs 8 and 9, $\mathbf{G}(\mathbf{p})$ is an $N \times M$ matrix whose element il is the derivative of the predicted data $d_i(\mathbf{p}, m_0, z_0)$ (Eq. 2) with respect to the l th element p_l of the parameter vector \mathbf{p} (Eq. 1), $l = 1, \dots, M$. Details about the constraint functions $\varphi_\ell(\mathbf{p})$, $\ell = 1, \dots, 7$, as well as the numerical procedure to solve this nonlinear inverse problem are given in the following sections.

2.3 Constraint functions

To explain the constraint functions $\varphi_\ell(\mathbf{p})$ (Eq. 3), $\ell = 1, \dots, 7$, used here to obtain stable solutions and introduce prior information about the magnetic source, we have organized them into the following three groups.

2.3.1 Smoothness constraints

This group is formed by variations of the first-order Tikhonov regularization (Aster et al. 2019, p. 103) that imposes smoothness on the radii r_j^k and the Cartesian coordinates x_0^k and y_0^k of the origin O^k , $j = 1, \dots, V$, $k = 1, \dots, L$, defining the horizontal section of each prism (Fig. 1b). They were proposed by Oliveira Jr. et al. (2011) and Oliveira Jr. & Barbosa (2013) and play a very important role in introducing prior information about the shape of the source.

The first constraint of this group is the *smoothness constraint on the adjacent radii defining the horizontal section of each prism*. This constraint imposes that adjacent radii r_j^k and r_{j+1}^k within each prism must be close to each other. It forces the estimated prism to be approximately cylindrical. Mathematically, the constraint is given by

$$\begin{aligned} \varphi_1(\mathbf{p}) &= \sum_{k=1}^L \left[(r_V^k - r_1^k)^2 + \sum_{j=1}^{V-1} (r_j^k - r_{j+1}^k)^2 \right] \\ &= \mathbf{p}^\top \mathbf{R}_1^\top \mathbf{R}_1 \mathbf{p} , \end{aligned} \quad (10)$$

where

$$\mathbf{R}_1 = \begin{bmatrix} \mathbf{S}_1 & \mathbf{0}_{LV \times 1} \end{bmatrix}_{LV \times M} , \quad (11)$$

$$\mathbf{S}_1 = \mathbf{I}_L \otimes \begin{bmatrix} (\mathbf{I}_V - \mathbf{D}_V^\top) & \mathbf{0}_{V \times 2} \end{bmatrix}_{V \times (V+2)} , \quad (12)$$

$\mathbf{0}_{LV \times 1}$ is an $LV \times 1$ vector with null elements, \mathbf{I}_L is the identity matrix of order L , “ \otimes ” denotes the Kronecker product (Horn & Johnson 1991, p. 243), $\mathbf{0}_{V \times 2}$ is a $V \times 2$ matrix with null elements, \mathbf{I}_V

is the identity matrix of order V and \mathbf{D}_V^\top is the upshift permutation matrix of order V (Golub & Loan 2013, p. 20). The gradient and Hessian of function $\varphi_1(\mathbf{p})$ (Eq. 10) are given by:

$$\nabla \varphi_1(\mathbf{p}) = 2\mathbf{R}_1^\top \mathbf{R}_1 \mathbf{p} , \quad (13)$$

and

$$\mathbf{H}_1(\mathbf{p}) = 2\mathbf{R}_1^\top \mathbf{R}_1 . \quad (14)$$

The second constraint of this group is the *smoothness constraint on the adjacent radii of the vertically adjacent prisms*, which imposes that adjacent radii r_j^k and r_j^{k+1} within vertically adjacent prisms must be close to each other. This constraint forces the shape of all prisms to be similar to each other and is given by

$$\begin{aligned} \varphi_2(\mathbf{p}) &= \sum_{k=1}^{L-1} \left[\sum_{j=1}^V (r_j^{k+1} - r_j^k)^2 \right] , \\ &= \mathbf{p}^\top \mathbf{R}_2^\top \mathbf{R}_2 \mathbf{p} \end{aligned} \quad (15)$$

where

$$\mathbf{R}_2 = \begin{bmatrix} \mathbf{S}_2 & \mathbf{0}_{(L-1)V \times 1} \end{bmatrix}_{(L-1)V \times M} , \quad (16)$$

$$\mathbf{S}_2 = \left(\begin{bmatrix} \mathbf{I}_{L-1} & \mathbf{0}_{(L-1) \times 1} \end{bmatrix} - \begin{bmatrix} \mathbf{0}_{(L-1) \times 1} & \mathbf{I}_{L-1} \end{bmatrix} \right) \otimes \begin{bmatrix} \mathbf{I}_V & \mathbf{0}_{V \times 2} \end{bmatrix} , \quad (17)$$

$\mathbf{0}_{(L-1)V \times 1}$ is an $(L-1)V \times 1$ vector with null elements, $\mathbf{0}_{(L-1) \times 1}$ is an $(L-1) \times 1$ vector with null elements and \mathbf{I}_{L-1} is the identity matrix of order $L-1$. The gradient and Hessian of function $\varphi_2(\mathbf{p})$ (Eq. 15) are given by:

$$\nabla \varphi_2(\mathbf{p}) = 2\mathbf{R}_2^\top \mathbf{R}_2 \mathbf{p} , \quad (18)$$

and

$$\mathbf{H}_2(\mathbf{p}) = 2\mathbf{R}_2^\top \mathbf{R}_2 . \quad (19)$$

The last constraint of this group is the *smoothness constraint on the horizontal position of the arbitrary origins of the vertically adjacent prisms*. This constraint imposes that the estimated horizontal Cartesian coordinates (x_0^k, y_0^k) and (x_0^{k+1}, y_0^{k+1}) of the origins O^k and O^{k+1} of adjacent prisms must be close to each other. It forces the centers of the prisms to be vertically aligned. This constraint is given by

$$\begin{aligned} \varphi_3(\mathbf{p}) &= \sum_{k=1}^{L-1} \left[(x_0^{k+1} - x_0^k)^2 + (y_0^{k+1} - y_0^k)^2 \right] , \\ &= \mathbf{p}^\top \mathbf{R}_3^\top \mathbf{R}_3 \mathbf{p} \end{aligned} \quad (20)$$

where

$$\mathbf{R}_3 = \begin{bmatrix} \mathbf{S}_3 & \mathbf{0}_{(L-1)2 \times 1} \end{bmatrix}_{(L-1)2 \times M}, \quad (21)$$

$$\mathbf{S}_3 = \left(\begin{bmatrix} \mathbf{I}_{L-1} & \mathbf{0}_{(L-1) \times 1} \end{bmatrix} - \begin{bmatrix} \mathbf{0}_{(L-1) \times 1} & \mathbf{I}_{L-1} \end{bmatrix} \right) \otimes \begin{bmatrix} \mathbf{0}_{2 \times V} & \mathbf{I}_2 \end{bmatrix}, \quad (22)$$

$\mathbf{0}_{(L-1)2 \times 1}$ is an $(L-1)2 \times 1$ vector with null elements, $\mathbf{0}_{2 \times V}$ is a $2 \times V$ matrix with null elements and \mathbf{I}_2 is the identity matrix of order 2. The gradient and Hessian of function $\varphi_3(\mathbf{p})$ (Eq. 20) are given by:

$$\nabla \varphi_3(\mathbf{p}) = 2\mathbf{R}_3^\top \mathbf{R}_3 \mathbf{p}, \quad (23)$$

and

$$\mathbf{H}_3(\mathbf{p}) = 2\mathbf{R}_3^\top \mathbf{R}_3. \quad (24)$$

2.3.2 Equality constraints

This group is formed by two constraints that were proposed by Oliveira Jr. et al. (2011) and Oliveira Jr. & Barbosa (2013) by following the same approach proposed Barbosa et al. (1997) and Barbosa et al. (1999a). They introduce a priori information about the shallowest prism and are suitable for outcropping sources.

The *source's outcrop constraint* imposes that the horizontal cross-section of the shallowest prism must be close to known outcropping boundary of the geologic source. The horizontal cross-section of the known outcropping boundary separating the geologic source from the host rock is described by the radii $\tilde{r}_1^0 \dots \tilde{r}_V^0$. Mathematically, this constraint is given by

$$\begin{aligned} \varphi_4(\mathbf{p}) &= \left[\sum_{j=1}^V (r_j^1 - \tilde{r}_j^0)^2 \right], \\ &= (\mathbf{R}_4 \mathbf{p} - \mathbf{a})^\top (\mathbf{R}_4 \mathbf{p} - \mathbf{a}) \end{aligned} \quad (25)$$

where \mathbf{a} is a $V \times 1$ vector containing the radii of the polygon defining the outcropping boundary

$$\mathbf{a} = \begin{bmatrix} \tilde{r}_1^0 & \dots & \tilde{r}_V^0 \end{bmatrix}^\top, \quad (26)$$

and

$$\mathbf{R}_4 = \begin{bmatrix} \mathbf{I}_V & \mathbf{0}_{V \times (M-V)} \end{bmatrix}_{V \times M}, \quad (27)$$

where \mathbf{I}_V is the identity matrix of order V and $\mathbf{0}_{V \times (M-V)}$ is a $V \times (M-V)$ matrix with null elements. The gradient and Hessian of function $\varphi_4(\mathbf{p})$ (Eq. 25) are given by:

$$\nabla \varphi_4(\mathbf{p}) = 2\mathbf{R}_4^\top (\mathbf{R}_4 \mathbf{p} - \mathbf{a}), \quad (28)$$

and

$$\mathbf{H}_4(\mathbf{p}) = 2\mathbf{R}_4^T \mathbf{R}_4 . \quad (29)$$

The *source's horizontal location constraint* imposes that the horizontal Cartesian coordinates of the origin within the shallowest prism must be as close as possible to a known outcropping point given by the horizontal Cartesian coordinates $(\tilde{x}_0^0, \tilde{y}_0^0)$. This constraint is given by

$$\begin{aligned} \varphi_5(\mathbf{p}) &= \left[(x_0^1 - \tilde{x}_0^0)^2 + (y_0^1 - \tilde{y}_0^0)^2 \right] , \\ &= (\mathbf{R}_5 \mathbf{p} - \mathbf{b})^T (\mathbf{R}_5 \mathbf{p} - \mathbf{b}) \end{aligned} \quad (30)$$

where \mathbf{b} is a 2×1 vector containing the horizontal Cartesian coordinates of the outcropping point

$$\mathbf{b} = \begin{bmatrix} \tilde{x}_0^0 & \tilde{y}_0^0 \end{bmatrix}^T , \quad (31)$$

and

$$\mathbf{R}_5 = \begin{bmatrix} \mathbf{0}_{2 \times V} & \mathbf{I}_2 & \mathbf{0}_{2 \times (M-V-2)} \end{bmatrix}_{2 \times M} , \quad (32)$$

where $\mathbf{0}_{2 \times (M-V-2)}$ is a $2 \times (M-V-2)$ matrix with null elements. The gradient and Hessian of function $\varphi_5(\mathbf{p})$ (Eq. 30) are given by:

$$\nabla \varphi_5(\mathbf{p}) = 2\mathbf{R}_5^T (\mathbf{R}_5 \mathbf{p} - \mathbf{b}) , \quad (33)$$

and

$$\mathbf{H}_5(\mathbf{p}) = 2\mathbf{R}_5^T \mathbf{R}_5 . \quad (34)$$

2.3.3 Minimum Euclidean norm constraints

Two constraints use the zeroth-order Tikhonov regularization with the purpose of obtaining stable solutions without introducing prior information about the shape of the source. However, these two constraints combined with the interpretation model impose source compactness.

The *Minimum Euclidean norm of the radii* imposes that all estimated radii within each prism must be close to null values. This constraint was proposed by Oliveira Jr. et al. (2011) and Oliveira Jr. & Barbosa (2013) and can be rewritten as follows

$$\begin{aligned} \varphi_6(\mathbf{p}) &= \sum_{k=1}^L \sum_{j=1}^V \left(r_j^k \right)^2 , \\ &= \mathbf{p}^T \mathbf{R}_6^T \mathbf{R}_6 \mathbf{p} \end{aligned} \quad (35)$$

where

$$\mathbf{R}_6 = \begin{bmatrix} \mathbf{S}_6 & \mathbf{0}_{(M-1) \times 1} \\ \mathbf{0}_{1 \times (M-1)} & 0 \end{bmatrix}_{M \times M} , \quad (36)$$

and

$$\mathbf{S}_6 = \mathbf{I}_L \otimes \begin{bmatrix} \mathbf{I}_V & \mathbf{0}_{V \times 2} \\ \mathbf{0}_{2 \times V} & \mathbf{0}_{2 \times 2} \end{bmatrix}_{(V+2) \times (V+2)}, \quad (37)$$

where $\mathbf{0}_{2 \times 2}$ is a 2×2 matrix with null elements, $\mathbf{0}_{V \times 2}$ is a $V \times 2$ matrix with null elements and $\mathbf{0}_{2 \times V}$ is a $2 \times V$ matrix with null elements. The gradient and Hessian of function $\varphi_6(\mathbf{p})$ (Eq. 35) are given by:

$$\nabla \varphi_6(\mathbf{p}) = 2\mathbf{R}_6^T \mathbf{R}_6 \mathbf{p}, \quad (38)$$

and

$$\mathbf{H}_6(\mathbf{p}) = 2\mathbf{R}_6^T \mathbf{R}_6. \quad (39)$$

The other constraint, the *Minimum Euclidean norm of the prism thickness*, imposes that the thickness of all prisms must be close to zero. We present this constraint to introduce a priori information about the maximum depth extent of the source which in turn is dependent on the depth to the top of the shallowest prism z_0 . It is given by

$$\begin{aligned} \varphi_7(\mathbf{p}) &= dz^2 \\ &= \mathbf{p}^T \mathbf{R}_7^T \mathbf{R}_7 \mathbf{p} \end{aligned}, \quad (40)$$

where

$$\mathbf{R}_7 = \begin{bmatrix} \mathbf{0}_{(M-1) \times (M-1)} & \mathbf{0}_{(M-1) \times 1} \\ \mathbf{0}_{1 \times (M-1)} & 1 \end{bmatrix}_{M \times M}. \quad (41)$$

The gradient and Hessian of function $\varphi_7(\mathbf{p})$ (Eq. 40) are given by:

$$\nabla \varphi_7(\mathbf{p}) = 2\mathbf{R}_7^T \mathbf{R}_7 \mathbf{p}, \quad (42)$$

and

$$\mathbf{H}_7(\mathbf{p}) = 2\mathbf{R}_7^T \mathbf{R}_7. \quad (43)$$

2.4 Computational procedures

In this section, we present the computational procedures to solve the nonlinear inverse problem for estimating a parameter vector $\hat{\mathbf{p}}_{(f)}$ that minimizes the goal function $\Gamma(\mathbf{p}, m_0, z_0)$ (Eq. 3), subject to the inequality constraints (Eq. 4), for previously defined values of depth to the top of the shallowest prism z_0 and total-magnetization intensity m_0 . We use an iterative gradient-based algorithm for solving the nonlinear inverse problem.

This section is divided into four parts. The first part describes how to define the number of prisms L , the number of vertices V , total-magnetization direction and thickness dz of all prisms, the initial

approximation $\hat{\mathbf{p}}_{(0)}$ for the parameter vector \mathbf{p} (Eq. 1), as well as the upper and lower limits in the inequality constraints (p_l^{min} and p_l^{max} in Eq. 4). All these variables are previously defined by the interpreter and never updated in the nonlinear inverse problem. The second part of this section explains how we define different tentative values for the depth to the top z_0 and total-magnetization intensity m_0 , as well as how we choose their optimum values. In the third part we present the gradient-based algorithm for solving the nonlinear inverse problem for a given tentative pair (m_0, z_0) . Finally, we describe how to set the weights α_ℓ (Eq. 3) in the fourth part of this section.

2.4.1 Initial approximation $\hat{\mathbf{p}}_{(0)}$ and inequality constraints

Our initial approximation $\hat{\mathbf{p}}_{(0)}$ is a uniformly-magnetized cylinder-like body formed by L prisms, all of them with the same number of vertices V . The radii of the vertices of all prisms ($r_j^k, j = 1, \dots, V, k = 1, \dots, L$) have the same constant value, so that the initial approximation approaches a vertical cylinder. The number of prisms L and vertices V are set based on the expected complexity of the magnetic source. We start by computing the reduction to pole (RTP) anomaly, which has three purposes. The first one is verifying if the used total-magnetization direction is valid. The second purpose is defining the upper and lower limits of the inequality constraints (Eq. 4). Finally, the third purpose of the RTP anomaly is defining the radius and horizontal Cartesian coordinates of the center of the cylinder-like initial approximation.

It is well known that if the source has a uniform magnetization direction, the RTP anomaly is predominantly positive and decays to zero close to its horizontal boundaries (e.g., Blakely 1996, p. 331). To compute this transformation, however, the interpreter must use declination and inclination values close to those defining the true total-magnetization direction of the source. Hence, the interpreter can validate the total-magnetization direction of the source by verifying if the computed RTP anomaly shows predominantly positive values.

By using the computed RTP anomaly, we also define the upper and lower limits (p_l^{min} and p_l^{max} in Eq. 4) for the parameters representing the radii r_j^k of the vertices and the horizontal coordinates x_0^k and y_0^k of the origins O^k of all prisms ($j = 1, \dots, V, k = 1, \dots, L$). For the parameters representing the radii r_j^k , the lower limit p_l^{min} is close to zero and the upper limit p_l^{max} is approximately defined by the radius of a circular area encompassing the region where the RTP anomaly is positive and decays to zero. The lowermost and uppermost x - and y -coordinates of this circular area are used to define, respectively, the lower and upper limits for the horizontal coordinates x_0^k and y_0^k .

Next, we set the same thickness dz for all prisms so that the resulting total thickness ($L dz$) is greater than that we expect for the true source. The lower and upper limits (p_l^{min} and p_l^{max} in Eq. 4) for the parameter dz are set to be, respectively, a value close to zero and a large value resulting in

a total thickness ($L dz$) greater than that we expect for the true source. At this point, we have fully defined the vector $\hat{\mathbf{p}}_{(0)}$ representing the cylinder-like initial approximation for the parameter vector \mathbf{p} (Eq. 1).

2.4.2 Definition of optimum values for m_0 and z_0

After defining the initial approximation $\hat{\mathbf{p}}_{(0)}$, we need to set the depth to the top of the shallowest prism z_0 and the total-magnetization intensity m_0 for all prisms. These two parameters are also previously defined by the interpreter and remain fixed along the iterations of our gradient-based algorithm for solving the nonlinear inverse problem.

In the absence of a priori information, the finding of values close to the true ones for z_0 and m_0 is a very difficult task due to the inherent ambiguity in magnetic inversion. It is expected that estimated magnetic sources obtained by using different combinations of z_0 and m_0 may produce similar data fits. Because of that, we do not estimate their values in the nonlinear inverse problem. Instead, we set ranges of tentative values for them. For each tentative pair (m_0, z_0) , we use the same previously defined cylinder-like initial approximation $\hat{\mathbf{p}}_{(0)}$ to obtain an independent estimated parameter vector $\hat{\mathbf{p}}_{(f)}$ minimizing the goal function $\Gamma(\mathbf{p}, m_0, z_0)$ (Eq. 3). Note that this approach results in a set of estimated magnetic sources with different depths to the top z_0 , total-magnetization intensities m_0 and geometries defined by different estimated parameter vectors $\hat{\mathbf{p}}_{(f)}$. Each estimated magnetic source results in a different value $\Gamma(\hat{\mathbf{p}}_{(f)}, m_0, z_0)$ for the goal function. On the discrete map of the goal function produced by the set of estimated magnetic sources, each one associated with a tentative pair (m_0, z_0) , we select the optimum values of m_0 and z_0 as those producing the smallest value of $\Gamma(\hat{\mathbf{p}}_{(f)}, m_0, z_0)$. We stress that all estimated parameter vectors $\hat{\mathbf{p}}_{(f)}$ are obtained by using the same values for the weights α_ℓ (Eq. 3). Details about how we set these weights are presented later, in the section *Setting the weights $\alpha_1 - \alpha_7$* .

Usually, the range of z_0 includes the topography ($z_0 = 0$) and the range of m_0 is based on a priori information such as petrophysical studies. In order to verify our initial approximation $\hat{\mathbf{p}}_{(0)}$ and the ranges of tentative values for z_0 and m_0 , we compute a discrete map of the data-misfit function $\phi(\mathbf{p}, m_0, z_0)$ (Eq. 5). All values in this map are produced by using the same previously defined initial approximation $\hat{\mathbf{p}}_{(0)}$. The only differences are the tentative values for z_0 and m_0 . The computation of this discrete map is carried out, before performing the inversions, with the purpose of verifying if there is at least one pair of m_0 and z_0 associated with a data-misfit function $\phi(\hat{\mathbf{p}}_{(0)}, m_0, z_0)$ showing a relatively low value. This means that the initial approximation $\hat{\mathbf{p}}_{(0)}$ and tentative values for m_0 and z_0 produce a predicted data vector $\mathbf{d}(\hat{\mathbf{p}}_{(0)}, m_0, z_0)$ close to the observed data vector \mathbf{d}^o . We stress that, at this step, we do not need a good data fit. However, if we cannot identify any point on the

discrete map of the data-misfit function $\phi(\hat{\mathbf{p}}_{(0)}, m_0, z_0)$ associated with a satisfactory data fit, the initial approximation $\hat{\mathbf{p}}_{(0)}$ and the ranges of z_0 and m_0 should be redefined before recomputing the discrete map.

2.4.3 Inversion algorithm for estimating \mathbf{p}

We use the Levenberg-Marquardt algorithm (e.g., Aster et al. 2019, p. 240) to solve the nonlinear inverse problem for estimating the parameter vector $\hat{\mathbf{p}}_{(f)}$ minimizing the goal function $\Gamma(\mathbf{p}, m_0, z_0)$ (Eq. 3), subject to the inequality constraints (Eq. 4), for given values of total-magnetization intensity m_0 and depth to the top of the shallowest prism z_0 . The Levenberg-Marquardt algorithm is an iterative gradient-based method that, at each iteration n , updates the estimate parameter vector $\hat{\mathbf{p}}_{(n)}$ to obtain a new estimated parameter vector $\hat{\mathbf{p}}_{(n+1)}$. We compute this update by following the same strategy of Barbosa et al. (1999b), Oliveira Jr. et al. (2011) and Oliveira Jr. & Barbosa (2013) to incorporate the inequality constraints (Eq. 4). This strategy consists in transforming each element $\hat{p}_l \in (p_l^{min}, p_l^{max})$ of the estimated parameter vector $\hat{\mathbf{p}}_{(n)}$ into the element $\hat{p}_l^\dagger \in (-\infty, +\infty)$ of an unconstrained vector $\hat{\mathbf{p}}_{(n)}^\dagger$ as follows:

$$\hat{p}_l^\dagger = -\ln \left(\frac{p_l^{max} - \hat{p}_l}{\hat{p}_l - p_l^{min}} \right), \quad (44)$$

where p_l^{min} and p_l^{max} are defined in the inequality constraints (Eq. 4). The inverse transformation of each element $\hat{p}_l^\dagger \in (-\infty, +\infty)$ into the element $\hat{p}_l \in (p_l^{min}, p_l^{max})$ is the following:

$$\hat{p}_l = p_l^{min} + \left(\frac{p_l^{max} - p_l^{min}}{1 + e^{-\hat{p}_l^\dagger}} \right). \quad (45)$$

At each iteration n of our algorithm, a correction $\Delta\hat{\mathbf{p}}_{(n)}^\dagger$ for the unconstrained vector $\hat{\mathbf{p}}_{(n)}^\dagger$ is computed by solving the following linear system:

$$\mathbf{Q}_{(n)}^{-1} \left[\mathbf{Q}_{(n)} \mathbf{H}^\dagger(\hat{\mathbf{p}}_{(n)}) \mathbf{Q}_{(n)} + \lambda_{(n)} \mathbf{I}_M \right] \mathbf{Q}_{(n)}^{-1} \Delta\hat{\mathbf{p}}_{(n)}^\dagger = -\nabla\Gamma(\hat{\mathbf{p}}_{(n)}), \quad (46)$$

where $\lambda_{(n)}$ is a positive scalar (known as Marquardt parameter) which is adjusted at each iteration and is associated with the Levenberg-Marquardt method (e.g., Silva et al. 2001; Aster et al. 2019, p. 240), \mathbf{I}_M is the identity matrix with order M , $\nabla\Gamma(\hat{\mathbf{p}}_{(n)})$ is the gradient of the goal function (Eq. 6), $\mathbf{H}^\dagger(\hat{\mathbf{p}}_{(n)})$ is a matrix given by

$$\mathbf{H}^\dagger(\hat{\mathbf{p}}_{(n)}) = \mathbf{H}(\hat{\mathbf{p}}_{(n)}) \mathbf{T}(\hat{\mathbf{p}}_{(n)}) \quad (47)$$

and $\mathbf{Q}_{(n)}$ is a diagonal matrix proposed by Marquardt (1963) for scaling the parameter $\lambda_{(n)}$ at each iteration. The element ll of this diagonal matrix is given by

$$q_{ll} = \frac{1}{\sqrt{h_{ll}^\dagger}}, \quad (48)$$

where h_{ll}^\dagger is the element ll of the matrix $\mathbf{H}^\dagger(\hat{\mathbf{p}}_{(n)})$ (Eq. 47). In Eq. 47, $\mathbf{H}(\hat{\mathbf{p}}_{(n)})$ is the Hessian matrix of the goal function (Eq. 7) and $\mathbf{T}(\hat{\mathbf{p}}_{(n)})$ is a diagonal matrix whose element ll is given by

$$t_{ll} = \frac{(p_l^{max} - \hat{p}_l + \epsilon)(\hat{p}_l - p_l^{min} + \epsilon)}{p_l^{max} - p_l^{min}}, \quad (49)$$

where \hat{p}_l is the l th element of the estimated parameter vector $\hat{\mathbf{p}}_{(n)}$ and ϵ is a small positive number ($\approx 10^{-2}$) used to prevent null values.

After estimating $\Delta\hat{\mathbf{p}}_{(n)}^\dagger$ by solving the linear system (Eq. 46), we update the unconstrained vector by computing

$$\hat{\mathbf{p}}_{(n+1)}^\dagger = \hat{\mathbf{p}}_{(n)}^\dagger + \Delta\hat{\mathbf{p}}_{(n)}^\dagger. \quad (50)$$

Next, we compute the elements of an updated parameter vector $\hat{\mathbf{p}}_{(n+1)}$ by using Eq. 45. Finally, we stop the iterative process by evaluating the invariance of the goal function (Eq. 3) along successive iterations. Specifically, we check if the inequality

$$\left| \frac{\Gamma(\hat{\mathbf{p}}_{(n+1)}, m_0, z_0) - \Gamma(\hat{\mathbf{p}}_{(n)}, m_0, z_0)}{\Gamma(\hat{\mathbf{p}}_{(n)}, m_0, z_0)} \right| \leq \tau \quad (51)$$

holds, where τ is a threshold value on the order of 10^{-3} to 10^{-4} . Usually, the inversion algorithm converges at 8-12 iterations. The estimate $\hat{\mathbf{p}}_{(n+1)}$ that is obtained at the last iteration and satisfies the inequality constraint defined by Eq. 51 is the estimated parameter vector $\hat{\mathbf{p}}_{(f)}$ minimizing the goal function $\Gamma(\mathbf{p}, m_0, z_0)$ (Eq. 3), for the given values of depth to the top z_0 and total-magnetization intensity m_0 . In the evaluation of the goal function, we compute the constraint functions $\varphi_\ell(\mathbf{p})$ (Eqs 10, 15, 20, 25, 30, 35 and 40), $\ell = 1, \dots, 7$, by using the expressions which are written as sum of terms instead of those defined by sparse matrices.

2.4.4 Choice of the weights α_ℓ

Attributing values to the weights α_ℓ (Eq. 3) is an important feature of our method. However, there is no analytical rule to define them and their values can be dependent on the particular characteristics of the type of geological setting where the method is being applied (Silva et al. 2001).

At this point, we draw attention that the weights α_ℓ (Eq. 3) are dimensional quantities. Note that the units of the data-misfit function (Eq. 5) and the constraint functions (Eqs 10, 15, 20, 25, 30, 35 and 40), are nT^2 and m^2 , respectively. Because we set the unit of the goal function (Eq. 3) as nT^2 , the unit of the weights α_ℓ (Eq. 3) is nT^2m^{-2} .

The physical dimensions of the weights α_ℓ makes assignment of their values problem dependent. To make these weights comparable to each other, we normalize the α_ℓ values as follows:

$$\alpha_\ell = \tilde{\alpha}_\ell \frac{E_\phi}{E_\ell}, \quad \ell = 1, \dots, 7, \quad (52)$$

where $\tilde{\alpha}_\ell$ is a positive scalar and E_ϕ/E_ℓ is a normalizing factor allowing the $\tilde{\alpha}_\ell$ to be independent of the physical units used. In Eq. 52, E_ℓ represents the trace of the Hessian matrix \mathbf{H}_ℓ (Eqs 14, 19, 24, 29, 34, 39, and 43) of the ℓ th constraining function $\varphi_\ell(\mathbf{p})$ (Eqs 10, 15, 20, 25, 30, 35, and 40). The constant E_ϕ is the trace of the Hessian matrix $\mathbf{H}_\phi(\hat{\mathbf{p}}_{(0)})$ (Eq. 9) of the misfit function $\phi(\mathbf{p})$ (Eq. 5) computed with the initial approximation $\hat{\mathbf{p}}_{(0)}$ for the parameter vector \mathbf{p} (Eq. 1) at the beginning of the inversion algorithm. Note that the trace of the Hessian matrix \mathbf{H}_ℓ is dimensionless and the trace of the Hessian matrix $\mathbf{H}_\phi(\hat{\mathbf{p}}_{(0)})$ has unit of nT^2m^{-2} . Thus, the positive scalars $\tilde{\alpha}_\ell$ in Eq. 52 are dimensionless quantities.

According to this empirical strategy, the weights α_ℓ (Eq. 3) are redefined using Eq. 52, in which the weights $\tilde{\alpha}_\ell$ are positive scalars, independent of physical units and less dependent on the particular characteristics of the interpretation geological setting.

The values attributed to the dimensionless weights $\tilde{\alpha}_1 - \tilde{\alpha}_7$ (Eq. 52) significantly impact the estimated models and cannot be automatically set without the interpreter's judgment. Based on our practical experience, we suggest some empirical procedures for setting these parameters.

The parameters $\tilde{\alpha}_1$ and $\tilde{\alpha}_2$ impose prior information on the shape of the horizontal cross-section of the prisms. The first one forces all prisms to have a circular horizontal cross-section, while the second forces all prisms to have a similar horizontal cross-section. Generally, their values vary from 10^{-5} to 10^{-3} and differ from each other by one order of magnitude, at most. The parameter $\tilde{\alpha}_3$ also varies from 10^{-5} to 10^{-3} and controls the relative position of adjacent prisms forming the model. A high value privileges a vertical estimated body, whereas a small value tends to generate an inclined estimated body.

In comparison to $\tilde{\alpha}_1$, $\tilde{\alpha}_2$ and $\tilde{\alpha}_3$, the other parameters usually have smaller values varying from 10^{-8} to 10^{-4} . The parameters $\tilde{\alpha}_4$ and $\tilde{\alpha}_5$ are used when a priori information about the source is available at the study area. The parameter $\tilde{\alpha}_6$ has a purely mathematical meaning and it is used only to obtain stable solutions for the inverse problem. Its value is set to be as small as possible. The parameter $\tilde{\alpha}_7$ controls the total-vertical extension of the the estimated body. The greater its value, the shallower the estimated depth to the bottom of the source will be and vice versa.

If the data fitting is poor or if the estimated source shows unrealistic shape, the dimensionless weights $\tilde{\alpha}_\ell$ (Eq. 52) must be fine-tuned to obtain a realistic solution. After tuning their values, they will be used in all inversions without changing along the iterations. The “educated guess” for $\tilde{\alpha}_4 = 0$ and $\tilde{\alpha}_5 = 0$ being set to zero seems strange in the case of a known outcrop. In that case, the non-zero constraints should add certainty to the inversion.

3 APPLICATION TO SYNTHETIC DATA

3.1 Simple model test

We have simulated a lopolithic intrusion, a funnel-shaped source (Cawthorn & Miller 2018), with simple geometry (blue prisms in Figs 3 and 4), which extends from $z_0 = 0$ m to 1 600 m along depth and satisfies most of the constraints described in subsection 2.3. It is formed by $L = 8$ prisms, all of them with the same number of vertices $V = 20$, thickness $dz = 200$ m and horizontal coordinates $(x_0^k, y_0^k) = (0, 0)$ m of the origins O^k , $k = 1, \dots, L$. The radii of all vertices are equal to each other within the same prism and decrease linearly with depth, varying from $r_j^0 = 1\,920$ m, at the shallowest prism, $r_j^L = 800$ m, at the deepest prism, $j = 1, \dots, V$. All prisms have the same total-magnetization direction with inclination -50° , declination 9° and intensity $m_0 = 9$ A/m. We calculated the total-field anomaly produced by this simple model, in an area of 100 km^2 area, by simulating an airborne survey composed of 21 flight lines that are equally spaced 500 m apart along the y -axis, at a constant vertical coordinate $z = -150$ m. At each line, there are 101 observation points spaced 100 m apart along x -axis. The main geomagnetic field direction simulated was -21.5° and -18.7° for the inclination and declination, respectively. The total-field anomaly is corrupted with a pseudorandom Gaussian noise having mean $\mu_0 = 0$ nT and standard deviation $\sigma_0 = 5$ nT (Fig. 3a).

We have inverted the noise-corrupted total-field anomaly (Fig. 3a) produced by the simulated lopolith-like body (blue prisms in Fig. 3b) and obtained 36 different estimates. Each estimate was obtained by using six different pairs of depth to the top z_0 and total-magnetization intensity m_0 . The ranges of z_0 and m_0 are shown in Fig. 3(c). Fig. 3(d) shows the RTP anomaly obtained from the noise-corrupted total-field anomaly (Fig. 3a). Note that the RTP anomaly exhibits predominantly positive values and decays to zero. As previously mentioned, the RTP anomaly is used to set up the initial approximation. The blue circle in Fig. 3(d) represents the horizontal projection of the initial approximation $\hat{\mathbf{p}}_{(0)}$ whose shape is a vertical cylinder. All estimates were generated by using the true values of total-magnetization inclination and declination, the same interpretation model formed by $L = 5$ prisms, each one with $V = 20$ vertices, and the same weights for the constraining functions: $\tilde{\alpha}_1 = 10^{-5}$, $\tilde{\alpha}_2 = 10^{-4}$, $\tilde{\alpha}_3 = 10^{-4}$, $\tilde{\alpha}_4 = 0$, $\tilde{\alpha}_5 = 0$, $\tilde{\alpha}_6 = 10^{-7}$, and $\tilde{\alpha}_7 = 10^{-6}$. In all inversions, the initial approximation $\hat{\mathbf{p}}_{(0)}$ (red prisms in Fig. 4b) has the same constant radii $r_j^k = 2\,000$ m, $k = 1, \dots, L$, $j = 1, \dots, V$, the same prism thicknesses $dz = 350$ m and the same origins $(x_0^k, y_0^k) = (0, 0)$ m for all prisms.

In a field data application, the unknown complexity of the real source can not be fully represented by the set of prisms forming the interpretative model. To approximate the synthetic test to a field data application, we define the initial approximation $\hat{\mathbf{p}}_{(0)}$ with a smaller number of parameters P than the

true source. We perform that by decreasing the number of prisms L and/or the number of vertices V . This is also a strategy applied to all synthetic tests to evaluate the robustness of the method.

Fig. 3(c) shows the discrete mapping of the goal functional $\Gamma(\hat{\mathbf{p}}_{(f)}, m_0, z_0)$ (Eq. 3) on the plane of the total-magnetization intensity (m_0) versus depth to the top (z_0). The true values of depth to the top z_0 and total-magnetization intensity m_0 (represented by the red triangle in Fig. 3c) produce the smallest value of goal function $\Gamma(\hat{\mathbf{p}}_{(f)}, m_0, z_0)$ (Eq. 3) and are taken as the optimum values. This estimated model (red prisms in Figs 4c and d) not only fits the noise-corrupted data (Fig. 4a), but also retrieves the geometry of the true model (blue prisms in Figs 4b-d). The inset in Fig. 4(a) shows that the residuals follow a normal distribution with mean μ and standard deviation σ compatible with those values used to generate the synthetic noise. The estimated thickness of each prism is $dz = 306.09$ m resulting in a depth-to-bottom estimate (1 530.42 m) very close to the true one (1 600 m). These results illustrate the good performance of our method in an ideal case.

3.2 Dipping model test

Fig. 5(a) shows the noise-corrupted total-field anomaly produced by an outcropping low-angle dipping volcanic duct (blue prisms in Figs 5c and d) embedded in nonmagnetic host rocks. The simulated magnetic data are contaminated with a pseudorandom Gaussian noise having mean $\mu_0 = 0$ nT and standard deviation $\sigma_0 = 5$ nT. We simulated airborne magnetic survey whose flight heights ranging from 0 to 720 m (Fig. 5b) and resulting in a total of 1 694 measurements. The simulated dipping source has total-magnetization direction with inclination -50° , declination 9° and intensity $m_0 = 12$ A/m. The main geomagnetic field direction has inclination of -21.5° and declination of -18.7° . To set up the simulated dipping source (blue prisms in Figs 5c and d), we used $L = 8$ prisms, all of them with the same number of vertices $V = 20$ and thickness $dz = 380$ m. The horizontal coordinates of the center of the shallowest prism that composes the simulated dipping source are $(x_0^1, y_0^1) = (-300, 600)$ m. The simulated dipping source has a top 0 m deep ($z_0 = 0$) and a base 3 040 m deep.

To set up the initial approximation and other variables in the inversion, we calculate the RTP anomaly (Fig. 6a) of the noise-corrupted total-field anomaly (Fig. 5a). Fig. 6(b) shows the goal function (Eq. 3) on the plane $z_0 \times m_0$ produced by 36 estimates obtained with a grid of 6×6 tentative values of depth to the top z_0 and total-magnetization intensity m_0 .

All 36 estimates were generated by using the true values of total-magnetization inclination and declination, the same interpretation model formed by $L = 5$ prisms, each one with $V = 20$ vertices, and the same weights for the constraining functions: $\tilde{\alpha}_1 = 10^{-3}$, $\tilde{\alpha}_2 = 10^{-3}$, $\tilde{\alpha}_3 = 10^{-6}$, $\tilde{\alpha}_4 = 0$, $\tilde{\alpha}_5 = 0$, $\tilde{\alpha}_6 = 10^{-6}$, and $\tilde{\alpha}_7 = 10^{-5}$.

The optimum solution is the one that produces the smallest value of the discrete mapping of the

goal function $\Gamma(\hat{\mathbf{p}}_{(f)}, m_0, z_0)$ (Fig. 6b). The white diamond in Fig. 6(b) pinpoints the minimum of the goal function $\Gamma(\hat{\mathbf{p}}_{(f)}, m_0, z_0)$ which is achieved when the estimated body has a top 20 m deep and a total-magnetization intensity of 12 A/m. Note that the depth to the top of the estimated body is deeper than the true one; however, the total-magnetization intensity was retrieved correctly.

Fig. 7(a) shows the magnetic-data residuals, defined as the difference between the synthetic noise-corrupted magnetic data in Fig. 5(a) and the predicted data (not shown). Fig. 7(b) shows the simulated dipping source (blue prisms) and the cylinder-like initial approximation (red prisms) with thickness $dz = 800$ m and the same origins $(x_0^k, y_0^k) = (-200, 0)$ m for all prisms. Note that the estimated source (red prisms in Figs. 7c and d) with $z_0 = 20$ m and $m_0 = 12$ A/m (pinpointed as the white diamond in Fig. 6b) retrieved the shape of the simulated dipping source (blue prisms) reasonably, although the retrieved depth to the bottom of 3 452.97 m was deeper than the true one. The retrieved deep-bottomed dipping source is probably influenced by a depth to the top z_0 deeper than the true one.

3.3 Dipping model in the presence of a regional field test

We analyze the ability of the proposed method to retrieve the geometry of the source in a simulated real-world scenario, where the observed total-field anomaly is produced not only by the magnetized source but also by a regional field. Here, the magnetized source to be retrieved has the same shape (blue prisms in Figs 5c and d) and magnetization direction of the previous test. In this test, the noise-corrupted total-field anomaly to be inverted (Fig. 8a) is obtained by adding a simulated regional field (Fig. 8b), represented by a first-order polynomial, to a simulated residual field (Fig. 5a) due to outcropping low-angle dipping volcanic duct (blue prisms in Figs 5c and d).

To remove the regional field from the original data (Fig. 8a), we perform a regional-residual separation by fitting a first-order polynomial to the original data using the least-squares method. Fig. 8(c) shows the residual total-field anomaly after subtracting from the original anomaly a regional total-field anomaly (Fig. 8d) obtained by a least-squares polynomial fitting.

We invert the anomaly over the area delimited by the magenta rectangle shown in Fig. 8(c). This anomaly to be inverted is called residual total-field anomaly and it is shown in Fig. 9(a). Because we expect that this anomaly is due to the dipping model (blue prisms in Figs. 5c and d), we calculate the differences (Fig. 9b) between the total-field anomaly produced by the dipping model (Fig. 5a) and the residual total-field anomaly (Fig. 9a) after a regional-residual separation using a least-squares polynomial fitting. Note that over the source the differences are less than 0.8% of the amplitude of the data due to the dipping model. Fig. 9(c) shows the RTP anomaly of the residual total-field anomaly shown in 9(a) that is used to set up the cylinder-like initial approximation. We perform 36 inversions by setting the same control variables of the previous test. The 36 estimates yield the discrete mapping

of the goal function $\Gamma(\hat{\mathbf{p}}_{(f)}, m_0, z_0)$ (Eq. 3) on the plane $z_0 \times m_0$ shown in Fig. 9(d). The smallest value of this goal function $\Gamma(\hat{\mathbf{p}}_{(f)}, m_0, z_0)$ (white diamond) pinpoints the optimum pair of z_0 and m_0 . By comparing the retrieved values of z_0 and m_0 (white diamond) and the true ones (red triangle), we can note an ambiguity involving these variables. In this test, the retrieved depth to the top of 40 m is deeper than the true one and the retrieved total-magnetization intensity of 15 A/m is higher than the true one.

Although there is an ambiguity involving z_0 and m_0 , the small residuals (Fig. 10a) indicate a reasonable fit of the inverted total-field anomaly (Fig. 9a). In all 36 inversions, we used the same cylinder-like initial approximation (red prisms in Fig. 10b). By assigning $z_0 = 40$ m and $m_0 = 15$ A/m (pinpointed as the white diamond in Fig. 9d), the estimated source (red prisms in Figs. 10c and d) recovers the shape of the simulated dipping source (blue prisms in Figs. 10b-d) reasonably.

3.4 Complex model test

Here, we have simulated a complex high-angle dipping intrusion (blue prisms in Figs 11 and 13) inspired by an alkaline vertical dipping intrusion. The simulated intrusion extends from $z_0 = 130$ m to 6130 m along depth. It is formed by $L = 10$ prisms, all of them with the same number of vertices $V = 30$ of thickness $dz = 600$ m. The horizontal coordinates of the origins O^k vary linearly from $(x_0^0, y_0^0) = (-250, 250)$ m, at the shallowest prism, to $(x_L^0, y_L^0) = (250, -750)$ m, at the deepest prism. This ensemble of 10 vertically juxtaposed prisms, exhibiting horizontal displacements between them, form a dyke-like intrusion, dipping at a high angle to the northwest (blue prisms in Figs 11 and 13). The radii defining the vertices of these prisms, $r_j^k, k = 1, \dots, L, j = 1, \dots, V$, vary from 240 m to 1540 m and also differ from each other within the same prism. All prisms have a constant total magnetization with inclination -50° , declination 9° and intensity $m_0 = 12$ A/m. We stress that the shape of the simulated complex model (blue prisms in Figs 11 and 13) violates severely two constraints described in subsection 2.3: $\varphi_1(\mathbf{p})$ (Eq. 10) and $\varphi_2(\mathbf{p})$ (Eq. 15). The violation of these constraints can be viewed by the nonsmoothness feature of the adjacent radii defining the horizontal section of each vertical prism and by the nonsmoothness feature of the adjacent radii of the vertically adjacent prisms.

We calculate the total-field anomaly produced by this complex model, in an area of 100 km², by simulating an airborne survey composed of 18 north-south flight lines distributed from -5000 m to 5000 m along the y -axis and a single east-west tie line approximately located at $x = 0$ m. The data points are located on the undulated surface shown in Fig. 11(a). Notice that both flight and tie lines are not perfectly straight. To compute the synthetic total-field anomaly, we consider a constant main geomagnetic field with inclination -21.5° and declination -18.7° . Finally, we have contaminated

the synthetic total-field anomaly with an additive pseudorandom Gaussian noise having mean and standard deviation equal to 0 nT and 5 nT, respectively (Fig. 11a).

To set up the cylinder-like initial approximation, we calculate the RTP anomaly (Fig. 12a) of the noise-corrupted total-field anomaly (Fig. 11a). We have inverted the noise-corrupted total-field anomaly produced by the complex model by using 36 different pairs of depth to the top z_0 and total-magnetization intensity m_0 (Fig. 12b). Differently from the previous simulations, in this test, the grid of m_0 and z_0 does not contain the true ones (represented by the red triangle in Fig. 12b). All the 36 estimates, obtained considering a grid of 6×6 tentative values of z_0 and m_0 (shown in Fig. 12b), use: i) the true magnetization direction of the simulated complex model (i.e., -50° , declination 9°), ii) the same interpretation model formed by $L = 8$ prisms, each one with $V = 20$ vertices, iii) the same cylinder-like initial approximation, and iv) the same weights for the constraining functions: $\tilde{\alpha}_1 = 10^{-5}$, $\tilde{\alpha}_2 = 10^{-4}$, $\tilde{\alpha}_3 = 10^{-4}$, $\tilde{\alpha}_4 = 0$, $\tilde{\alpha}_5 = 0$, $\tilde{\alpha}_6 = 10^{-7}$, and $\tilde{\alpha}_7 = 10^{-6}$.

Fig. 12(b) shows the goal function $\Gamma(\hat{\mathbf{p}}_{(f)}, m_0, z_0)$ (Eq. 3), with different total-magnetization intensity m_0 and depth-to-the-top z_0 , on the plane $(m_0 \times z_0)$. We note that a well-defined minimum region the goal function $\Gamma(\hat{\mathbf{p}}_{(f)}, m_0, z_0)$ (dark blue region) contains the true pair of $z_0 = 130$ m and $m_0 = 12$ A/m (red triangle) and the optimum pair of $z_0 = 150$ m and $m_0 = 12.6$ A/m (white diamond), which yields the smallest value of the goal function $\Gamma(\hat{\mathbf{p}}_{(f)}, m_0, z_0)$ and retrieves the estimated model.

Fig. 13(a) shows the residuals defined as the difference between the synthetic noise-corrupted magnetic data in Fig. 11(a) and the predicted data (not shown). The cylinder-like initial approximation ($\hat{\mathbf{p}}_{(0)}$), shown in Fig. 13(b) by the red prisms, is composed by a set of eight prisms, has the same constant radii $r_j^k = 800$ m, $k = 1, \dots, 8$, $j = 1, \dots, 20$, the same thickness $dz = 650$ m and the same origin $(x_0^k, y_0^k) = (-300, 300)$ m for all prisms of the interpretation model.

Figs. 13(c) and (d) show the estimated model (red prisms) obtained by using $z_0 = 150$ m and $m_0 = 12.6$ A/m (white diamond in Fig. 12b). Note that the this estimated model fits the noise-corrupted data (small residuals in Fig. 13a) and also retrieves the geometry of the true source (blue prisms in Figs. 13b-d). The inset in Fig. 13(a) shows that the residuals follow a normal distribution with mean μ and standard deviation σ compatible with those values used to generate the noise-corrupted data. The estimated of depth to the bottom (5 904.45 m) and volume (11.19 km³) are underestimated, but still close to the true values (6 130 m and 12.60 km³). These results show that our method can also be very useful to interpret complex sources, even if they do not perfectly satisfy the constraints imposed to solve the nonlinear inverse problem.

4 APPLICATION TO FIELD DATA

We have applied our method to interpret airborne magnetic data provided by Geological Survey of Brazil (CPRM) over the Anitápolis complex, in southern Brazil. The airborne survey was flown with north-south and east-west lines spaced by 500 m and 10 000 m from each other, respectively. The total-field anomaly data (Fig. 14a) were corrected from diurnal correction and the main geomagnetic field using the IGRF. The inclination, declination, and intensity of the main geomagnetic field at the study area, for the period of the survey, are -37.05° , -18.17° and $\approx 22\,768$ nT, respectively. Fig. 14(b) shows a regional field obtained by fitting, in the least-squares sense, a first-order polynomial to the original data (Fig. 14a). Figs 14(c) and 14(d) show the geometric height. We have subtracted 800 m from their values and, after the inversion, the estimated model is corrected.

After removing a first-order polynomial (Fig. 14b) from the original data (Fig. 14a) using a least-squares polynomial fitting, we obtain the residual total-field anomaly shown in Fig. 15(a). The Anitápolis alkaline-carbonatitic complex forms a circular concentric body ($\approx 6\text{ km}^2$ in area) containing magnetite as part of its mineralogical composition. It intruded into the Late Proterozoic leucogranites of the Dom Feliciano mobile belt in the Early Cretaceous (132 Ma), apparently concomitant with the voluminous flood tholeiitic basalts of the Serra Geral Formation (133–130 Ma) at the southern side of the Paraná Basin (Gibson et al. 1999; Scheibe et al. 2005). As pointed out by Gomes et al. (2018), there is still some debate about the emplacement of the Anitápolis alkaline-carbonatitic complex. Melcher & Coutinho (1966) pointed out the influence of N-S-trending faults. Horbach & Marimon (1980) affirmed that the Anitápolis complex is controlled by a large N30W lineament. Scheibe et al. (2005) considered that it is roughly emplaced along the E-W Rio Uruguay Lineament. According to Riccomini et al. (2005), the Anitápolis complex does not show a clear structural control.

By using the methodology of Reis et al. (2020), we set the total-magnetization direction of the interpretation model with inclination $I = -21^\circ$ and declination $D = -11^\circ$. These values were estimated by Reis et al. (2019). We have accepted this estimated magnetization direction because the calculated RTP anomaly (Fig. 15b) of the residual total-field anomaly (Fig. 15a) is predominantly positive and decays to zero toward the borders of the study area (Reis et al. 2020, 2019).

This total-magnetization direction indicates the presence of remanent magnetization. Laboratory measurements on rock samples obtained at the Jacupiranga complex, another alkaline complex located northward of the study area, with the same age as the Anitápolis complex, show total-magnetization intensities values varying from approximately 0.01 to 29.90 A/m (Alva-Valdivia et al. 2009, tb. 1). We used these values as a priori information to set the range of possible values for the total-magnetization intensity m_0 in the Anitápolis complex.

We used an interpretation model formed by $L = 6$ prisms, each one with $V = 20$ vertices defining

their horizontal cross-sections. We inverted the residual total-field anomaly (Fig. 15a) for each pair of m_0 and z_0 shown in Fig. 15(c), resulting in 100 estimated models. For all models, we set the same initial approximation $\hat{\mathbf{p}}_{(0)}$ (red prisms in Figs 16b and 17b) with origin at $(x_0^k, y_0^k) = (6921, 688)$ km, constant radii $r_j^k = 700$ m for all vertices forming all prisms and the same constant thickness $dz = 900$ m. We also set the same weights which were used in the synthetic tests, i.e., $\tilde{\alpha}_1 = 10^{-4}$, $\tilde{\alpha}_2 = 10^{-3}$, $\tilde{\alpha}_3 = 10^{-4}$, $\tilde{\alpha}_4 = 0$, $\tilde{\alpha}_5 = 0$, $\tilde{\alpha}_6 = 10^{-8}$, and $\tilde{\alpha}_7 = 10^{-5}$ (Eq. 52). Fig. 15(c) shows that there is a region (blue region) containing candidate solutions producing small values of the goal function $\Gamma(\hat{\mathbf{p}}_{(f)}, m_0, z_0)$ (Eq. 3), with different values of m_0 and z_0 . Two estimates produced the smallest values for $\Gamma(\hat{\mathbf{p}}_{(f)}, m_0, z_0)$ (Eq. 3). The magenta diamond in Fig. 15(c) represents the non-outcropping estimated model shown in Fig. 16. This model produces a reasonable data fit (Fig. 16a). It has a volume 6.94 km^3 , total thickness of 3045.69 m ($dz = 510.95$), depth-to-the-top $z_0 = 20 \text{ m}$ and total-magnetization intensity $m_0 = 16.0 \text{ A/m}$. The white diamond in Fig. 15(c) represents the outcropping estimated model shown in Fig. 17. This model is similar to that shown in Fig. 16. It has a volume 7.24 km^3 , total thickness 3032.65 m ($dz = 505.44$), depth-to-the-top $z_0 = 0 \text{ m}$ and total-magnetization intensity $m_0 = 15 \text{ A/m}$. In comparison with the non-outcropping model shown in Fig. 16, the alternative model shown in Fig. 17 has very similar geometry, but it outcrops.

Finally, we stress that both total-magnetization intensities $m_0 = 16 \text{ A/m}$ and $m_0 = 15 \text{ A/m}$ are within the range found by Alva-Valdivia et al. (2009) for intrusions located at the Jacupiranga complex. Both estimated models show a nearly N30W elongated body with high dip along depth (Figs 16 and 17), which coincides with the topographic low observed in Fig 14(c). Hence, these estimates agree with the interpretation proposed by Horbach & Marimon (1980), that considered the presence of N30W-trending fault controlling the Anitápolis complex.

5 CONCLUSIONS

We have developed a total-field anomaly nonlinear inversion to estimate the shape of an isolated 3-D geological body assuming the knowledge about its total-magnetization direction. We approximate the body by a set of vertically stacked right prisms. The horizontal cross-section of each prism is a polygon defined by a given number of equi-angularly spaced vertices from 0° to 360° . We perform our inversion for a set of tentative values for the depth to the top of the shallowest prism and the total-magnetization intensity of all prisms. For each tentative pair of depth to the top and total-magnetization intensity, our method estimates the geometries of the cross-sections (the radii associated with the polygon vertices), the thickness and the horizontal positions of the prisms. The estimated bodies producing the smallest values of the goal function form the set of candidate solutions. Our method is an extension of previous works developed for retrieving the geometry of 3-D bodies by inverting gravity and gravity-gradient data. We not only adapted the previous methods for interpreting total-field anomaly data, but also generalized them to include the depth to the top and depth extension of the prisms forming the interpretation model.

Results obtained with synthetic data produced by a simple symmetric source and by a realistic geological source, in the presence of regional field, with variable dip and shape with depth, show that our method is able to retrieve the shape of the source and fit the data in both cases. We applied our method to interpret a total-field anomaly data over the alkaline-carbonatitic complex of Anitápolis, in southern Brazil. We obtained two candidate models having similar shapes, depths to the top and total-magnetic intensities, all of them consistent with the available geological information. Both estimated models suggest that the emplacement of the Anitápolis complex seems to be controlled by a nearly N30W-trending fault in agreement with previous studies. It is important to bear in mind, however, the possible bias in the geometry of the estimated body due to errors in the total-magnetization direction used as a priori information.

Finally, we stress that our method is not strictly to invert the total-field anomaly; rather, it can be adapted to invert single and multiple magnetic field components. Possible extensions of this work is the inversion of elongated and/or multiple sources. In addition, the combination of gradient-based and heuristic optimization methods could be applied to estimate optimal regularization weights and overcome problems with local minima.

ACKNOWLEDGMENTS

The authors thank associate editor Jorg Renner, reviewers Horst Holstein, and Alexander Minakov for their questions and suggestions that greatly improved the original manuscript. We thank the Brazilian geological service CPRM for providing the field data. Leonardo Vital thanks the PhD. scholarship from CAPES (Finance Code 001). Vanderlei Oliveira Jr. thanks the fellowships from CNPQ (grant 308945/2017-4) and FAPERJ (grant E-26/202.729/2018). Valeria Barbosa thanks the fellowships from CNPQ (grant 307135 /2014-4) and FAPERJ (grant E-26/202.582/2019).

REFERENCES

- Abedi, M., Asghari, O., & Norouzi, G.-H., 2015. Collocated cokriging of iron deposit based on a model of magnetic susceptibility: a case study in Morvarid mine, Iran, *Arabian Journal of Geosciences*, **8**(4), 2179–2189.
- Alva-Valdivia, L. M., Perrin, M., Rivas-Sánchez, M. L., Goguitchaichvili, A., López-Loera, H., Lopes, O. F., & Bonás, T. B., 2009. Rock magnetism and microscopy of the Jacupiranga alkaline-carbonatitic complex, southern Brazil, *Earth, Planets and Space*, **61**(1), 161–171.
- Aster, R. C., Borchers, B., & Thurber, C. H., 2019. *Parameter Estimation and Inverse Problems*, Elsevier, 3rd edn.
- Ballantyne, E. J., 1980. Magnetic curve fit for a thin dike; calculator program (TI 59), *Geophysics*, **45**(3), 447–455.
- Barbosa, V. C. & Silva, J. B., 2006. Interactive 2d magnetic inversion: A tool for aiding forward modeling and testing geologic hypotheses, *Geophysics*, **71**(5), L43–L50.
- Barbosa, V. C. F., Silva, J. B. C., & Medeiros, W. E., 1997. Gravity inversion of basement relief using approximate equality constraints on depths, *Geophysics*, **62**, 1745–1757.
- Barbosa, V. C. F., Silva, J. B. C., & Medeiros, W. E., 1999a. Gravity inversion of a discontinuous relief stabilized by weighted smoothness constraints on depth, *Geophysics*, **64**(5), 1429–1437.
- Barbosa, V. C. F., Silva, J. B. C., & Medeiros, W. E., 1999b. Stable inversion of gravity anomalies of sedimentary basins with nonsmooth basement reliefs and arbitrary density contrast variations, *Geophysics*, **64**(3), 754–764.
- Bhattacharyya, B. K., 1980. A generalized multibody model for inversion of magnetic anomalies, *Geophysics*, **45**(2), 255–270.
- Blakely, R. J., 1996. *Potential Theory in Gravity and Magnetic Applications*, Cambridge University press.
- Caratori Tontini, F., Cocchi, L., & Carmisciano, C., 2006. Depth-to-the-bottom optimization for magnetic data inversion: Magnetic structure of the latium volcanic region, Italy, *Journal of Geophysical Research*, **111**, B11104.
- Cawthorn, R. & Miller, J., 2018. Lopolith – A 100 year-old term. Is it still definitive?, *South African Journal of Geology*, **121**(3), 253–260.

- Cella, F. & Fedi, M., 2012. Inversion of potential field data using the structural index as weighting function rate decay: Inversion of potential field data, *Geophysical Prospecting*, **60**(2), 313–336.
- Cribb, J., 1976. Application Of The Generalized Linear Inverse To The Inversion Of Static Potential Data, *Geophysics*, **41**(6), 1365–1369.
- Gibson, S. A., Thompson, R. N., Leonardos, O. H., Dickin, A. P., & Mitchell, J. G., 1999. The limited extent of plume-lithosphere interactions during continental flood-basalt genesis: geochemical evidence from cretaceous magmatism in southern Brazil, *Contributions to Mineralogy and Petrology*, **137**(1), 147–169.
- Golub, G. H. & Loan, C. F. V., 2013. *Matrix Computations (Johns Hopkins Studies in the Mathematical Sciences)*, Johns Hopkins University Press, 4th edn.
- Gomes, C. d. B., Comin-Chiaromonti, P., Azzone, R. G., Ruberti, E., & Rojas, G. E. E., 2018. Cretaceous carbonatites of the southeastern Brazilian Platform: a review, *Brazilian Journal of Geology*, **48**, 317 – 345.
- Hidalgo-Gato, M. C. & Barbosa, V. C. F., 2019. Fast 3d magnetic inversion of a surface relief in the space domain, *Geophysics*, **84**(5), J57–J67.
- Horbach, R. & Marimon, R. G., 1980. *Esboço da evolução tectônica e seu significado na gênese dos depósitos de fluorita no sudeste catarinense*, vol. 3, pp. 1540–1551, Sociedade Brasileira de Geologia, Camboriú, SC, Brazil.
- Horn, R. A. & Johnson, C. R., 1991. *Topics in Matrix Analysis*, Cambridge University Press, 1st edn.
- Last, B. J. & Kubik, K., 1983. Compact gravity inversion, *GEOPHYSICS*, **48**(6), 713–721.
- Li, W., Lu, W., Qian, J., & Li, Y., 2017. A multiple level-set method for 3d inversion of magnetic data, *Geophysics*, **82**(5), J61–J81.
- Li, Y. & Oldenburg, D. W., 1996. 3-D inversion of magnetic data, *Geophysics*, **61**(2), 394–408.
- Marquardt, D. W., 1963. An algorithm for least-squares estimation of nonlinear parameters, *Journal of the society for Industrial and Applied Mathematics*, **11**(2), 431–441.
- Medeiros, W. E. & Silva, J. B., 1995. Simultaneous estimation of total magnetization direction and 3-D spatial orientation, *GEOPHYSICS*, **60**(5), 1365–1377.
- Melcher, G. C. & Coutinho, J. M. V., 1966. Rochas alcalinas e carbonatito de Anitápolis, estado de Santa Catarina, *Boletim da Sociedade Brasileira de Geologia*, **15**(1), 59–93.
- Oliveira Jr., V. C. & Barbosa, V. C. F., 2013. 3-D radial gravity gradient inversion, *Geophysical Journal International*, **195**(2), 883–902.
- Oliveira Jr., V. C., Barbosa, V. C. F., & Silva, J. B. C., 2011. Source geometry estimation using the mass excess criterion to constrain 3-D radial inversion of gravity data, *Geophysical Journal International*, **187**(2), 754–772.
- Pignatelli, A., Nicolosi, I., & Chiappini, M., 2006. An alternative 3d inversion method for magnetic anomalies with depth resolution, *Annals of geophysics = Annali di geofisica*.
- Pilkington, M., 1997. 3-D magnetic imaging using conjugate gradients, *Geophysics*, **62**(4), 1132–1142.
- Pilkington, M., 2009. 3d magnetic data-space inversion with sparseness constraints, *Geophysics*, **74**(1), L7–L15.

- Plouff, D., 1976. Gravity and magnetic fields of polygonal prisms and application to magnetic terrain corrections, *Geophysics*, **41**(4), 727–741.
- Portniaguine, O. & Zhdanov, M. S., 1999. Focusing geophysical inversion images, *Geophysics*, **64**(3), 874–887.
- Portniaguine, O. & Zhdanov, M. S., 2002. 3-D magnetic inversion with data compression and image focusing, *Geophysics*, **67**(5), 1532–1541.
- Reis, A. L. A., Oliveira Jr., V. C., & Barbosa, V. C. F., 2019. Equivalent layer technique for estimating magnetization direction, *SEG Technical Program Expanded Abstracts 2019*, pp. 1769–1773.
- Reis, A. L. A., Oliveira Jr., V. C., & Barbosa, V. C. F., 2020. Generalized positivity constraint on magnetic equivalent layers, *GEOPHYSICS*, **85**(6), 1–12.
- Riccomini, C., Velázquez, V., & Gomes, C., 2005. Tectonic controls of the Mesozoic and Cenozoic alkaline magmatism in the central-southeastern brazilian platform, in *Mesozoic to Cenozoic Alkaline Magmatism in the Brazilian Platform*, chap. 2, pp. 31–55, eds Comin-Chiaromonti, P. & Gomes, C., Edusp/Fapesp, São Paulo.
- Scheibe, L., Furtado, S., Comin-Chiaromonti, P., & Gomes, C., 2005. Cretaceous alkaline magmatism from Santa Catarina state, southern Brazil, in *Mesozoic to Cenozoic Alkaline Magmatism in the Brazilian Platform*, chap. 16, pp. 523–571, eds Comin-Chiaromonti, P. & Gomes, C., Edusp/Fapesp, São Paulo.
- Shamsipour, P., Chouteau, M., & Marcotte, D., 2011. 3d stochastic inversion of magnetic data, *Journal of Applied Geophysics*, **73**(4), 336–347.
- Silva, J. B. C. & Hohmann, G. W., 1983. Nonlinear magnetic inversion using a random search method, *Geophysics*, **48**(12), 1645–1658.
- Silva, J. B. C., Medeiros, W. E., & Barbosa, V. C. F., 2001. Potential-field inversion: Choosing the appropriate technique to solve a geologic problem, *GEOPHYSICS*, **66**(2), 511–520.
- Uieda, L., Oliveira Jr., V. C., & Barbosa, V. C. F., 2013. Modeling the earth with Fatiando a Terra, in *Proceedings of the 12th Python in Science Conference*, pp. 96 – 103.
- Wang, X. & Hansen, R. O., 1990. Inversion for magnetic anomalies of arbitrary three-dimensional bodies, *Geophysics*, **55**(10), 1321–1326.

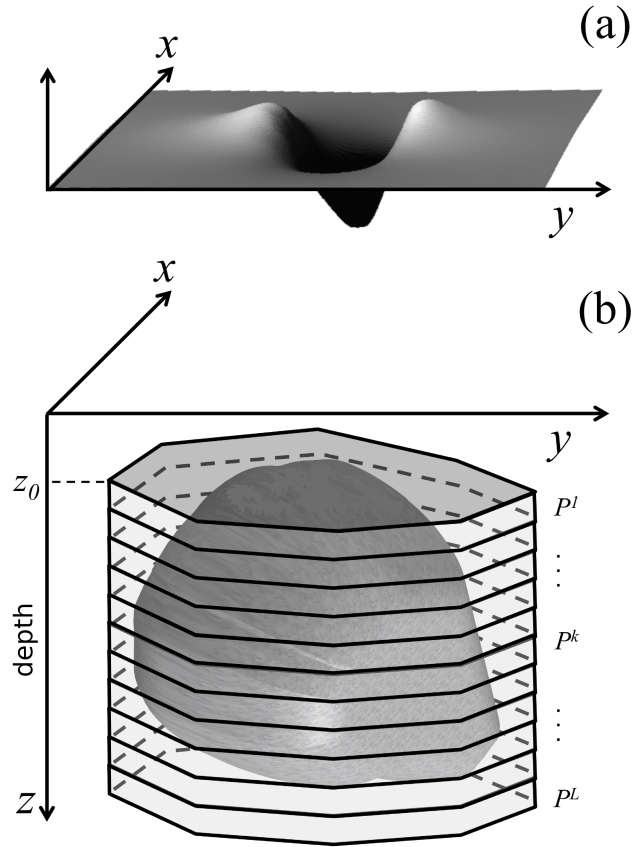


Figure 1. Schematic representation (modified from Oliveira Jr. & Barbosa (2013)) of (a) total-field anomaly (gray surface) produced by (b) a 3-D anomalous source (dark gray volume). The interpretation model in (b) consists of a set of L vertical, juxtaposed 3-D prisms (light gray) in the vertical direction of a right-handed coordinate system. At the initial iteration, the interpretation model is defined as a vertical cylinder.

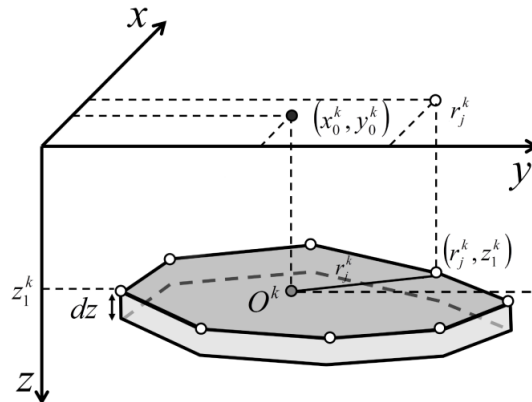


Figure 2. Polygonal cross-section of the k th vertical prism described by V vertices (white dots) with radii r_j^k , $j = 1, \dots, V$, $k = 1, \dots, L$, referred to an arbitrary origin O^k (grey dot) with horizontal Cartesian coordinates (x_0^k, y_0^k) , $k = 1, \dots, L$, (black dot).

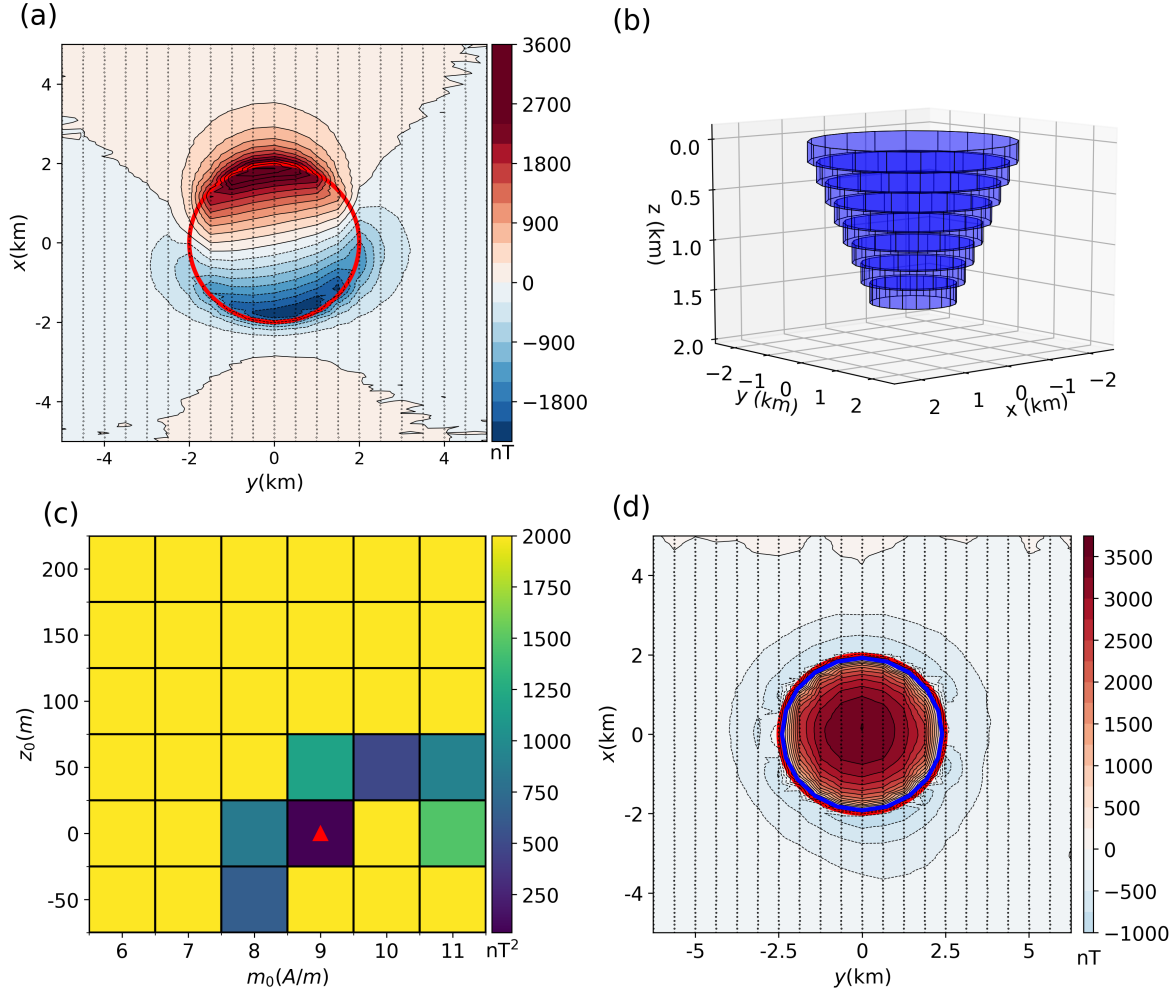


Figure 3. Simple model simulation. (a) Noise-corrupted total-field anomaly produced by the lopolithic-like body (blue prisms) shown in the panel (b). The black dots represent the observation points. The red circle represents the horizontal projection of the initial approximation $\hat{\mathbf{p}}_{(0)}$ (red prisms in Fig. 4b). (b) Perspective view of the simple model (lopolithic intrusion) represented by the blue prisms. (c) Discrete map of the goal function $\Gamma(\mathbf{p}, m_0, z_0)$ (Eq. 3) produced by the estimates $\hat{\mathbf{p}}_{(f)}$ obtained with a 6×6 grid of tentative values for depth to the top z_0 and total-magnetization intensity m_0 . The red triangle pinpoint the true and retrieved values of m_0 and z_0 . (d) RTP anomaly of the total-field anomaly shown in Fig. 3a.

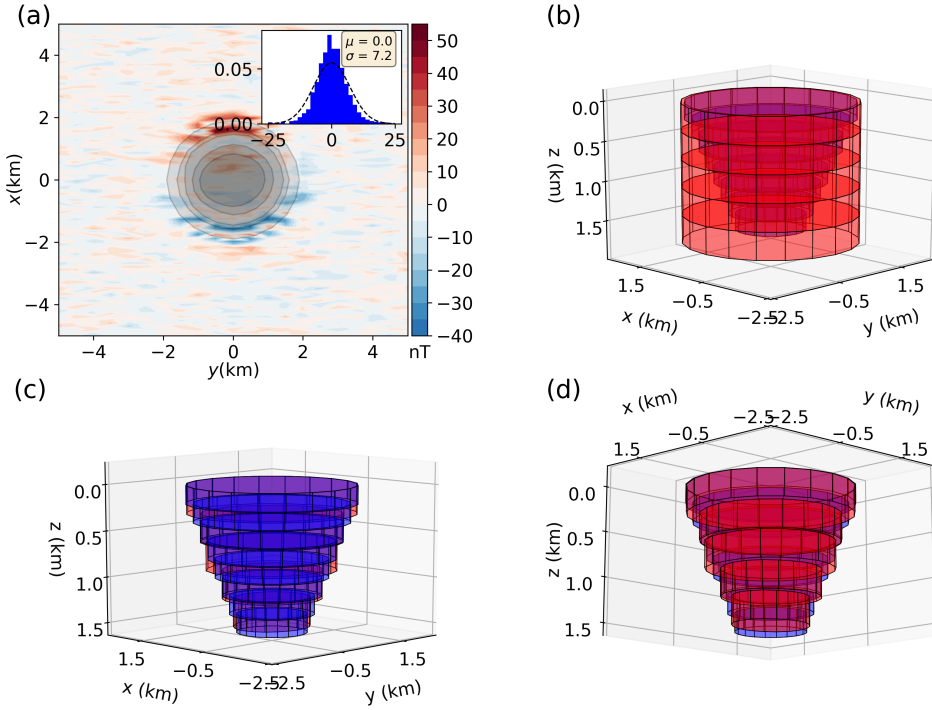


Figure 4. Simple model simulation. (a) Residuals between the noise-corrupted data (Fig. 3a) and the predicted data (not shown) produced by the estimated model (red prisms shown in the panels (c) and (d)). The inset shows the histogram of the residuals and the Gaussian curve (dashed line) has mean and standard deviation equal to $\mu = -0.04$ nT and $\sigma = 7.21$ nT, respectively. (b) Perspective views of the initial approximation (red prisms) and the true model (blue prisms). (c) and (d) Comparison between the estimated source (red prisms) and the true model (blue prisms) in perspective views.

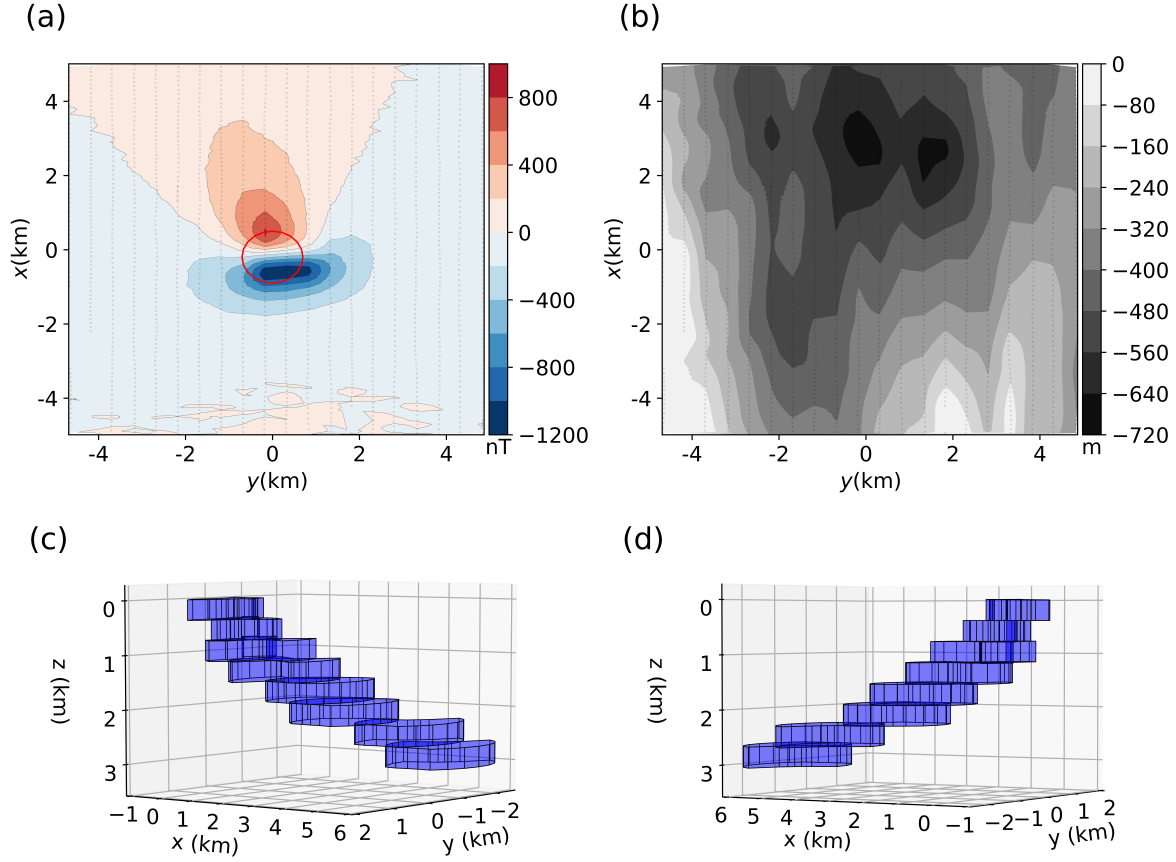


Figure 5. Dipping model simulation. (a) Noise-corrupted total-field anomaly produced by the dipping model (blue prisms shown in the panels (c) and (d)). The black dots represent the observation points. The red circle represents the horizontal projection of the initial approximation $\hat{\mathbf{p}}_{(0)}$ (red prisms in Fig. 7). The blue polygon is the horizontal projection of the simulated dipping source. (b) Geometric height of the observation points. (c) and (d) Perspective views of the dipping model represented by the blue prisms.

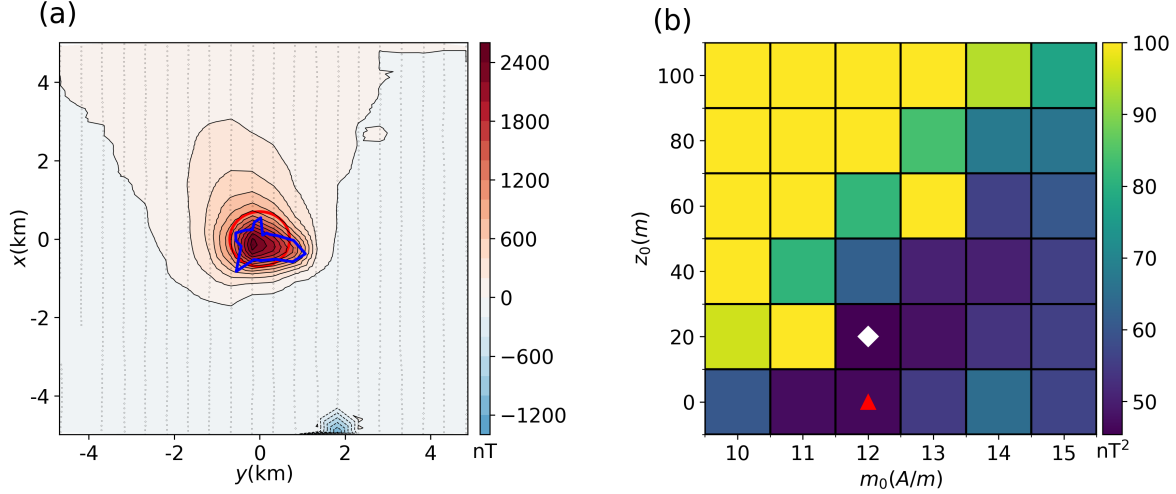


Figure 6. Dipping model simulation. (a) RTP anomaly of the total-field anomaly shown in Fig. 5(a). The red circle and the blue polygon represent the horizontal projections of the initial approximation $\hat{\mathbf{p}}_{(0)}$ and the simulated dipping source, respectively. (b) Discrete map of the goal function $\Gamma(\mathbf{p}, m_0, z_0)$ (Eq. 3) produced by the estimates $\hat{\mathbf{p}}_{(f)}$ obtained with a 6×6 grid of tentative values for depth to the top z_0 and total-magnetization intensity m_0 . The red triangle and white diamond pinpoint, respectively, the true and retrieved values of m_0 and z_0 .

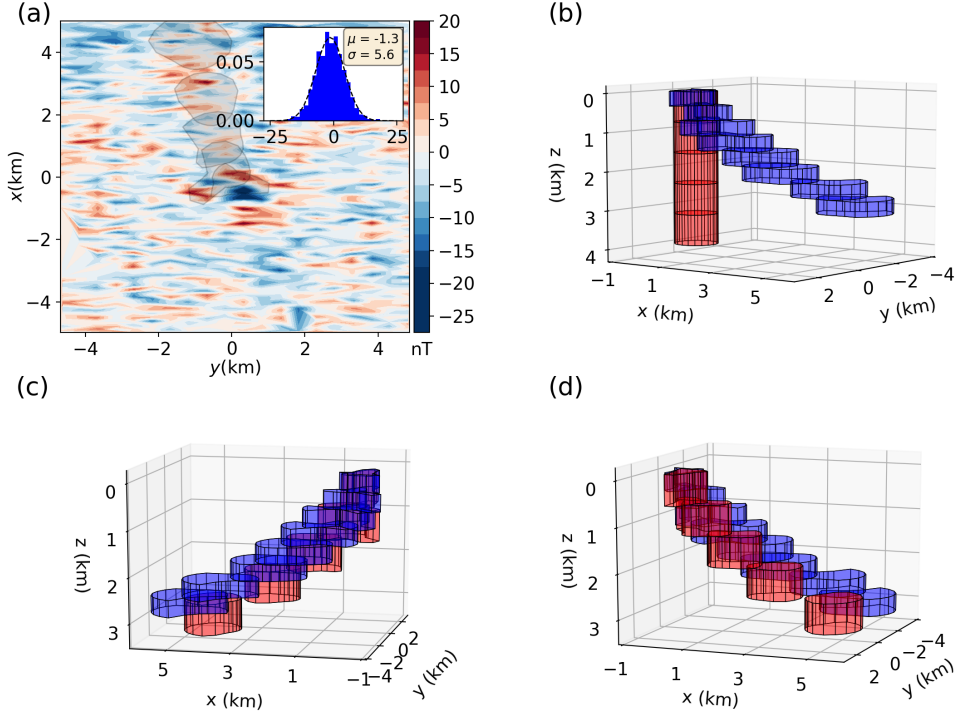


Figure 7. Dipping model simulation. (a) Residuals between the noise-corrupted data (Fig. 5a) and the predicted data (not shown) produced by the estimated model (red prisms shown in the panels (c) and (d)) using m_0 and z_0 pinpointed by the white diamond in Fig. 6b. The inset shows the histogram of the residuals and the Gaussian curve (dashed line) has mean and standard deviation equal to $\mu = 1.3$ nT and $\sigma = 5.6$ nT, respectively. The gray polygons are the horizontal projections of the estimated source (red prisms in panels (c) and (d)). (b) Perspective views of the initial approximation (red prisms) and the true model (blue prisms). (c) and (d) Comparison between the estimated source (red prisms) and the true model (blue prisms) in perspective views.

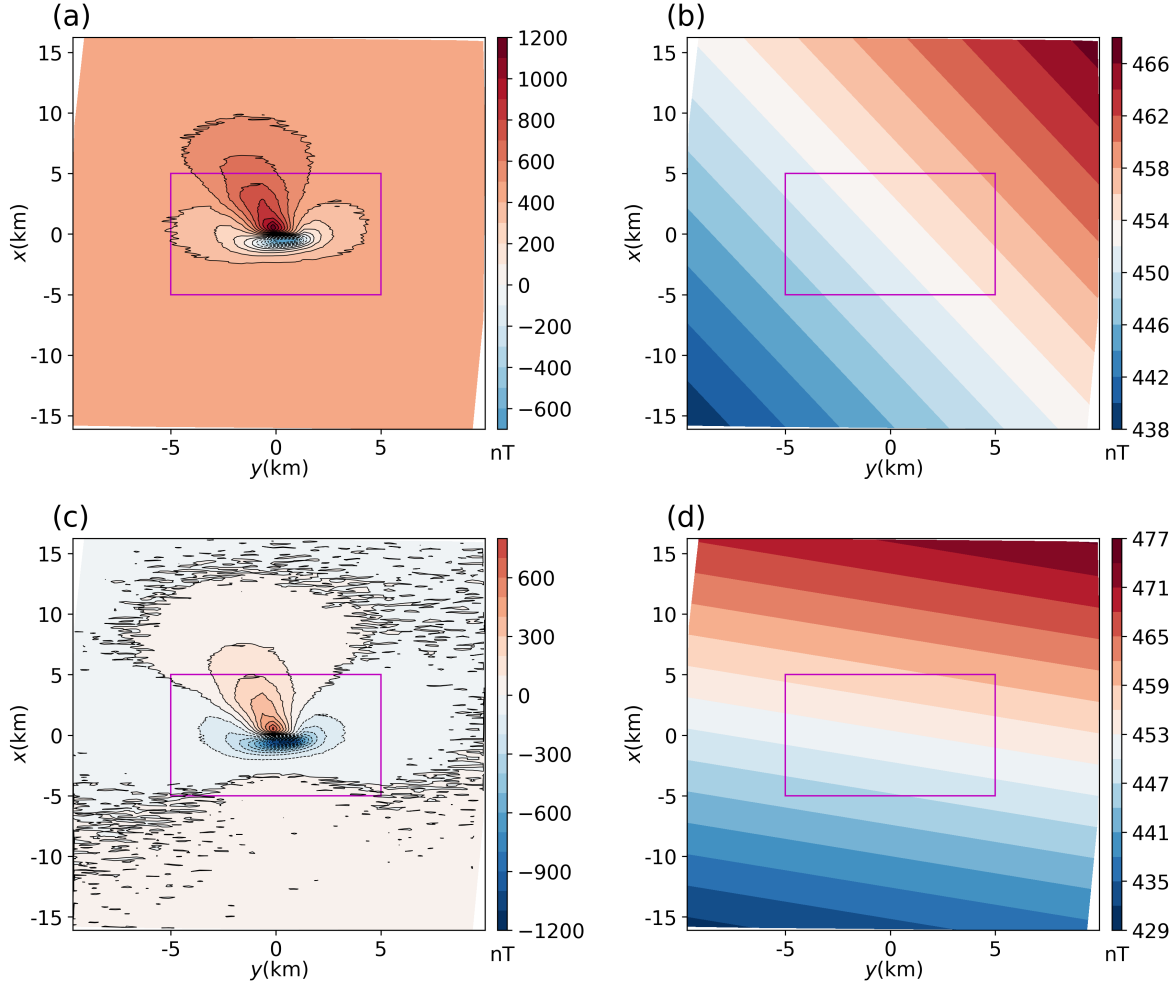


Figure 8. Dipping model with regional field simulation. (a) Noise-corrupted total-field anomaly composed of a simulated residual field (Fig. 5a) due to dipping model (blue prisms shown in Fig. 5c and d) and a regional field (shown in panel (b)). (b) Simulated regional field through a first-order polynomial. (c) Residual total-field anomaly after subtracting from the original anomaly (shown in panel (a)) a regional total-field anomaly (shown in panel (d)) obtained by a least-squares polynomial fitting. (d) Regional total-field anomaly approximated by a least-squares polynomial fitting to the original anomaly (shown in panel (a)). The magenta rectangle delimits the data to be inverted.

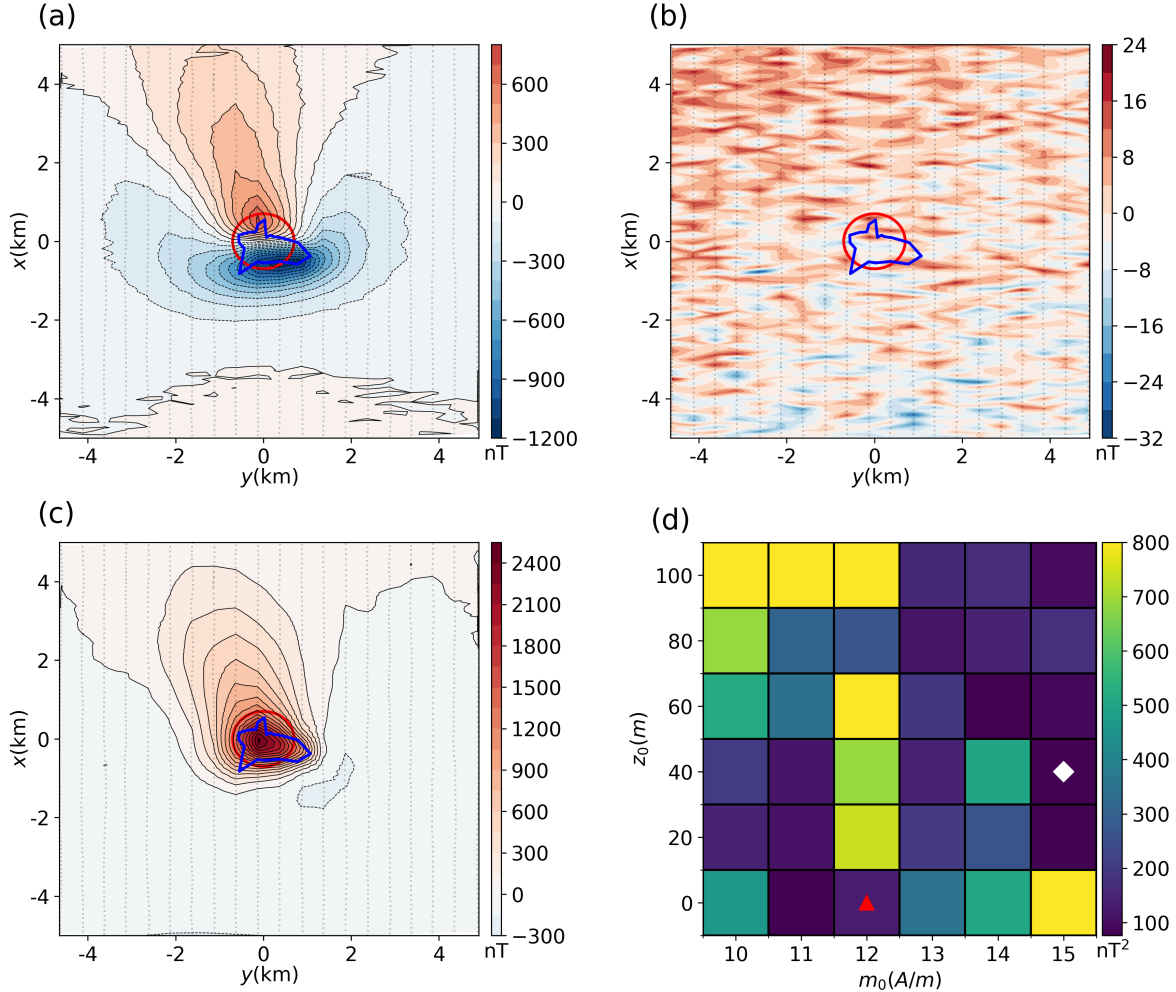


Figure 9. Dipping model with regional field simulation. (a) Residual total-field anomaly to be inverted over the area delimited by the magenta rectangle in Fig. 8(c). (b) Differences between the total-field anomaly produced by the dipping model (Fig. 5a) and the residual total-field anomaly (shown in panel (a)) after a regional-residual separation using a least-squares polynomial fitting. (c) RTP anomaly of the residual total-field anomaly shown in panel (a). (d) Discrete map of the goal function $\Gamma(\mathbf{p}, m_0, z_0)$ (Eq. 3) produced by the estimates $\hat{\mathbf{p}}_{(f)}$ obtained with a 6×6 grid of tentative values for depth to the top z_0 and total-magnetization intensity m_0 . The red triangle and white diamond pinpoint, respectively, the true and retrieved values of m_0 and z_0 . In the panels (a)-(c), the red circle and the blue polygon represent the horizontal projections of the initial approximation $\hat{\mathbf{p}}_{(0)}$ and the simulated dipping source, respectively.

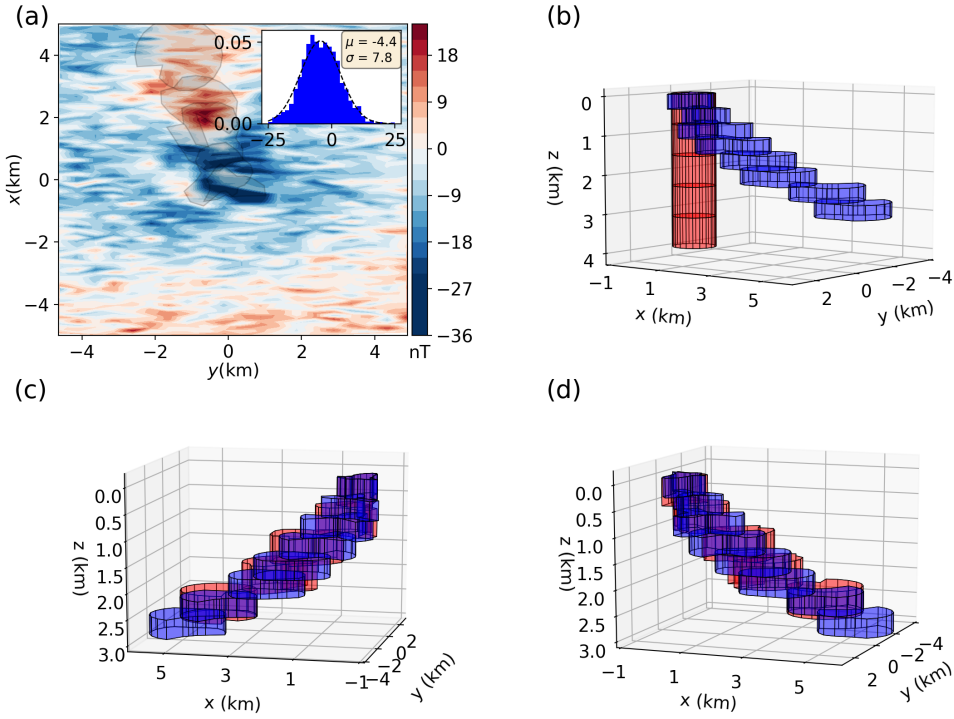


Figure 10. Dipping model with regional field simulation. (a) Residuals between the noise-corrupted data (Fig. 9a) and the predicted data (not shown) produced by the estimated model (red prisms shown in the panels (c) and (d)) using m_0 and z_0 pinpointed by the white diamond in Fig. 9d. The inset shows the histogram of the residuals and the Gaussian curve (dashed line) has mean and standard deviation equal to $\mu = -4.4$ nT and $\sigma = 7.8$ nT, respectively. The gray polygons are the horizontal projections of the estimated source (red prisms in panels (c) and (d)). (b) Perspective views of the initial approximation (red prisms) and the true model (blue prisms). (c) and (d) Comparison between the estimated source (red prisms) and the true model (blue prisms) in perspective views.

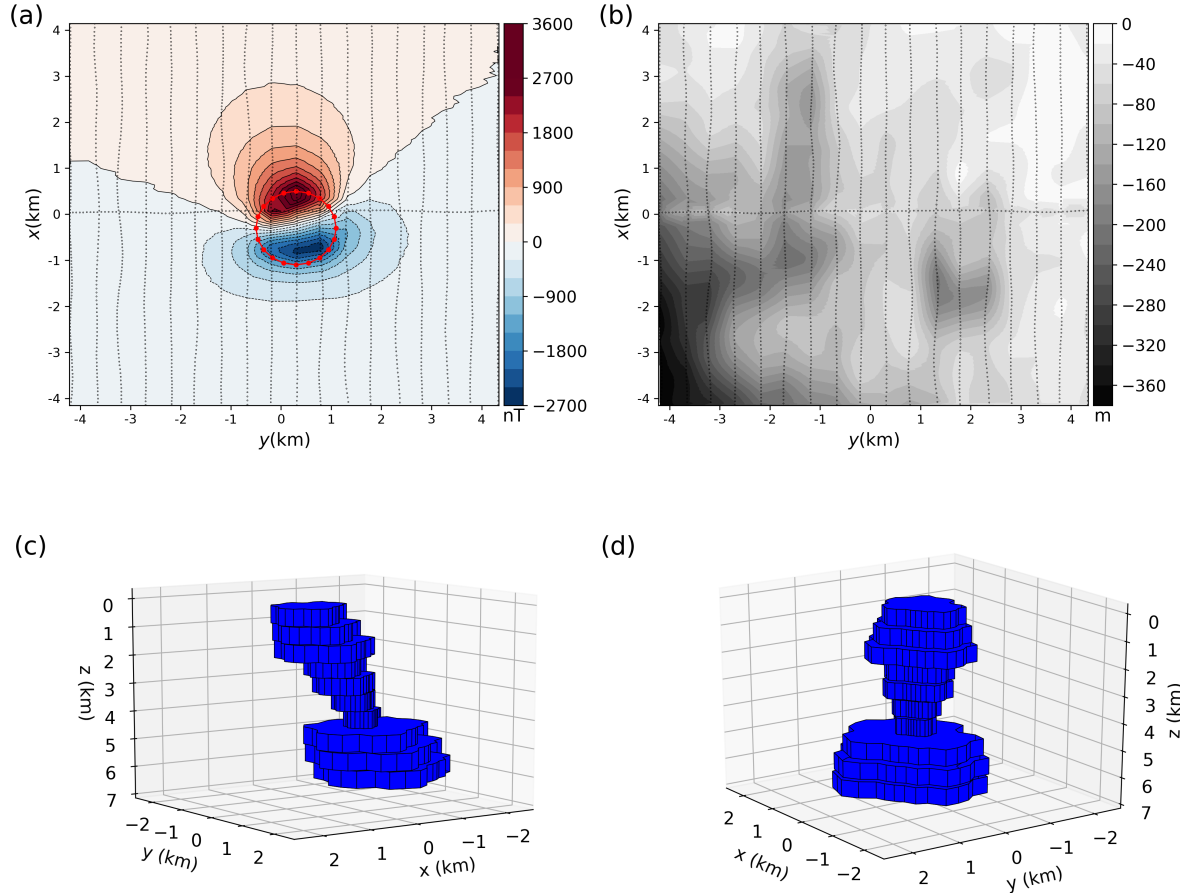


Figure 11. Complex model simulation. (a) Noise-corrupted total-field anomaly produced by the complex model (blue prisms shown in the panels (c) and (d)). The black dots represent the observation points. The connected red dots represent the horizontal projection of the initial approximation $\hat{\mathbf{p}}_{(0)}$ (red prisms in Fig. 13b). (b) Geometric height of the observation points. (c) and (d) Perspective views of the complex model represented by the blue prisms.

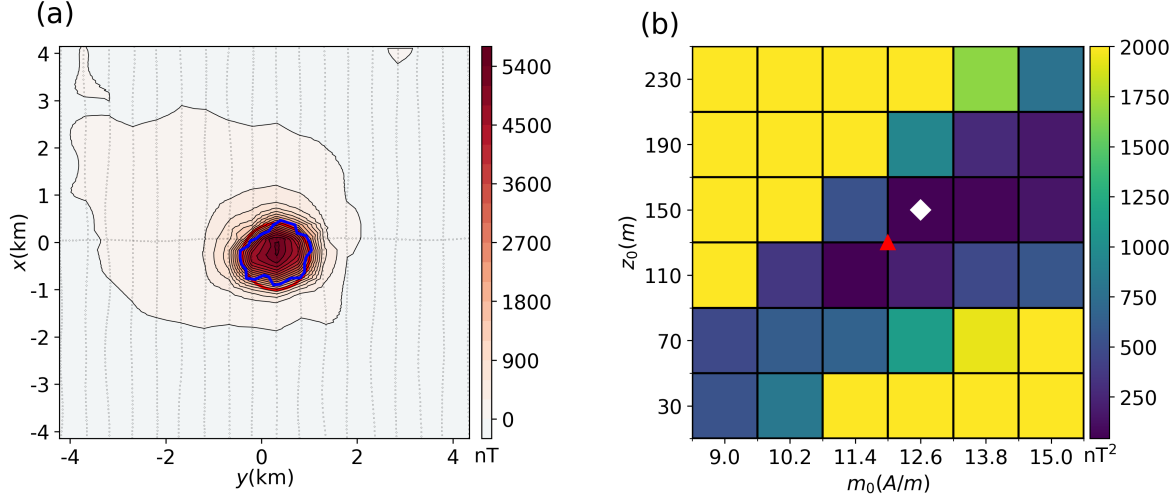


Figure 12. Complex model simulation. (a) RTP anomaly of the total-field anomaly shown in Fig. 11(a). The red circle and the blue polygon represent the horizontal projections of the initial approximation $\hat{\mathbf{p}}_{(0)}$ and the simulated dipping source, respectively. (b) Discrete map of the goal function $\Gamma(\mathbf{p}, m_0, z_0)$ (Eq. 3) produced by the estimates $\hat{\mathbf{p}}_{(f)}$ obtained with a 6×6 grid of tentative values for depth to the top z_0 and total-magnetization intensity m_0 . The red triangle and white diamond pinpoint, respectively, the true and retrieved values of m_0 and z_0 .

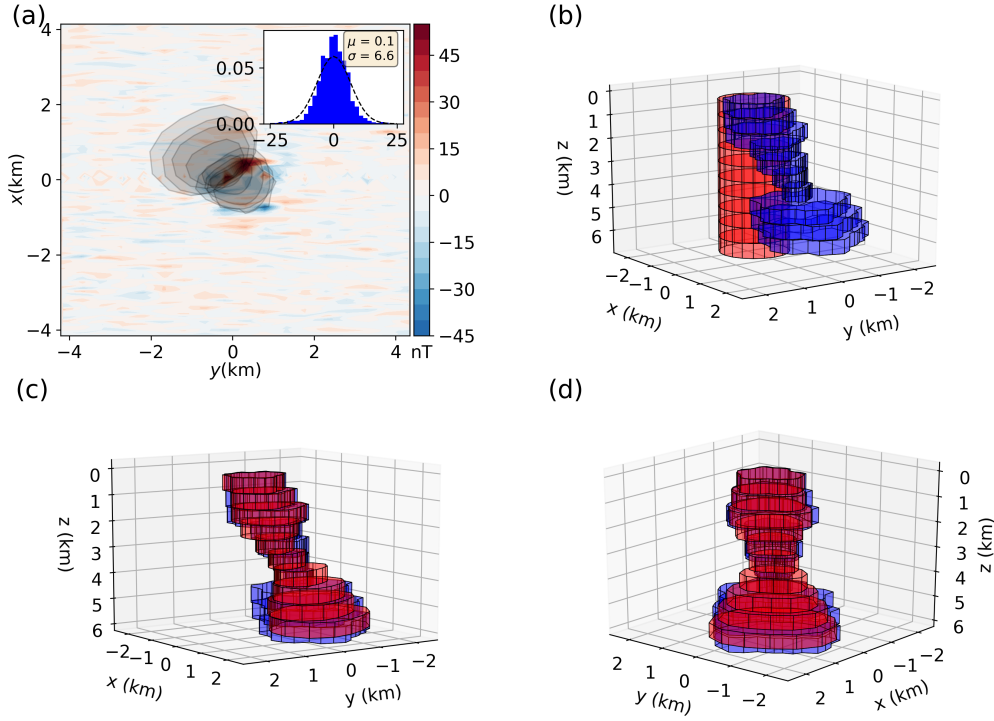


Figure 13. Complex model simulation. (a) Residuals between the noise-corrupted data (Fig. 11a) and the predicted data (not shown) produced by the estimated model (red prisms panels (c) and (d)) using m_0 and z_0 pinpointed by the white diamond in Fig. 12b. The inset shows the histogram of the residuals and the Gaussian curve (dashed line) has mean and standard deviation equal to $\mu = 0.01$ nT and $\sigma = 6.6$ nT, respectively. (b) Perspective view of the initial approximation (red prisms) and the true model (blue prisms). (c) and (d) Comparison between the estimated source (red prisms) and the true model (blue prisms) in perspective views.

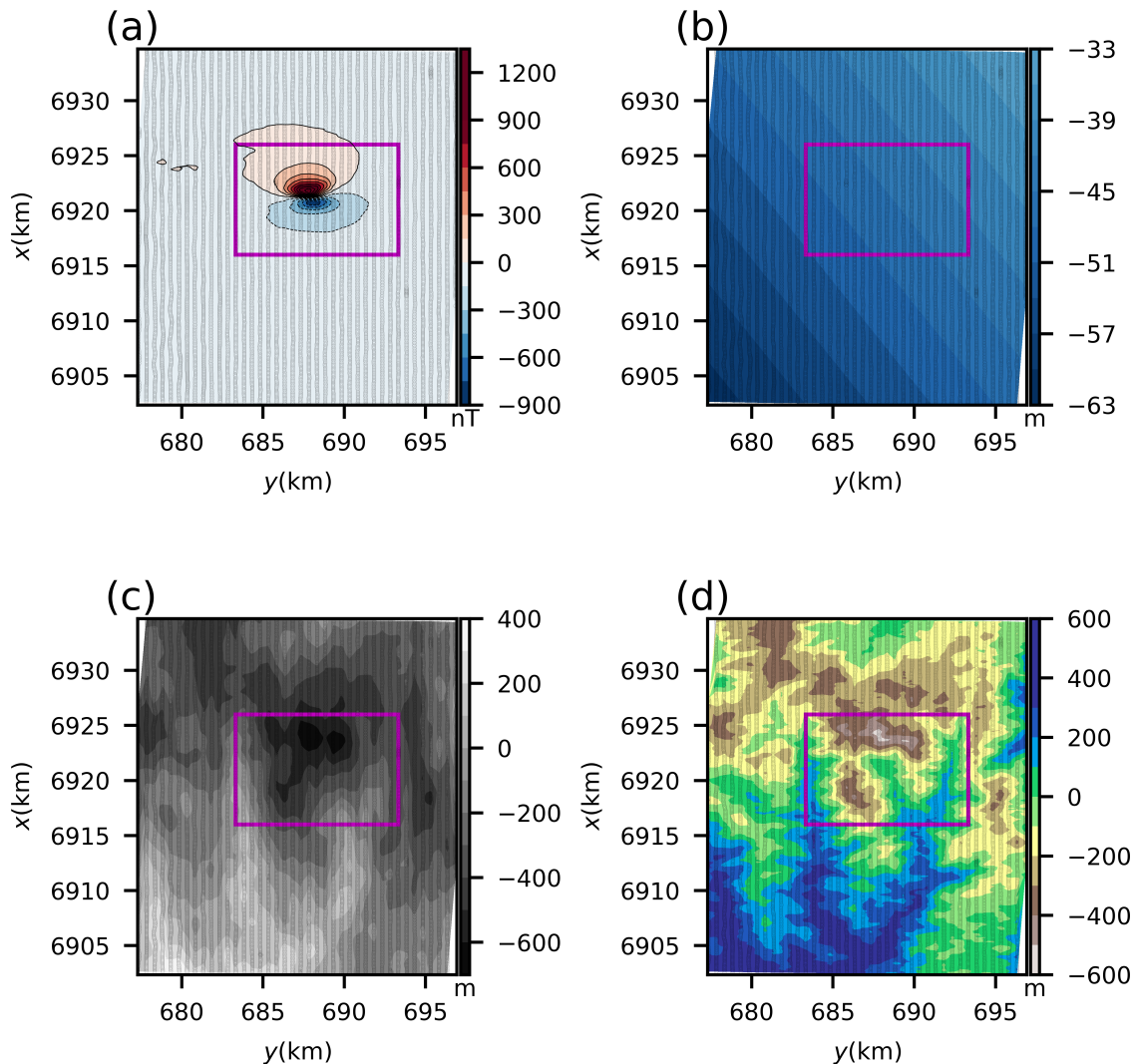


Figure 14. Application to field data. (a) Observed total-field anomaly over the Anitápolis alkaline-carbonatitic complex in southern Brazil. The horizontal UTM coordinates are referred to the central meridian 51° W. The black dots represent the observation points. (b) Regional field using least-squares first-order polynomial fitting. (c) Geometric height of the observation points. (d) Topography of the study area. Both of these coordinates are referred to the WGS84 ellipsoid. We have subtracted 800 m from their values. The magenta rectangle delimits the data to be inverted.

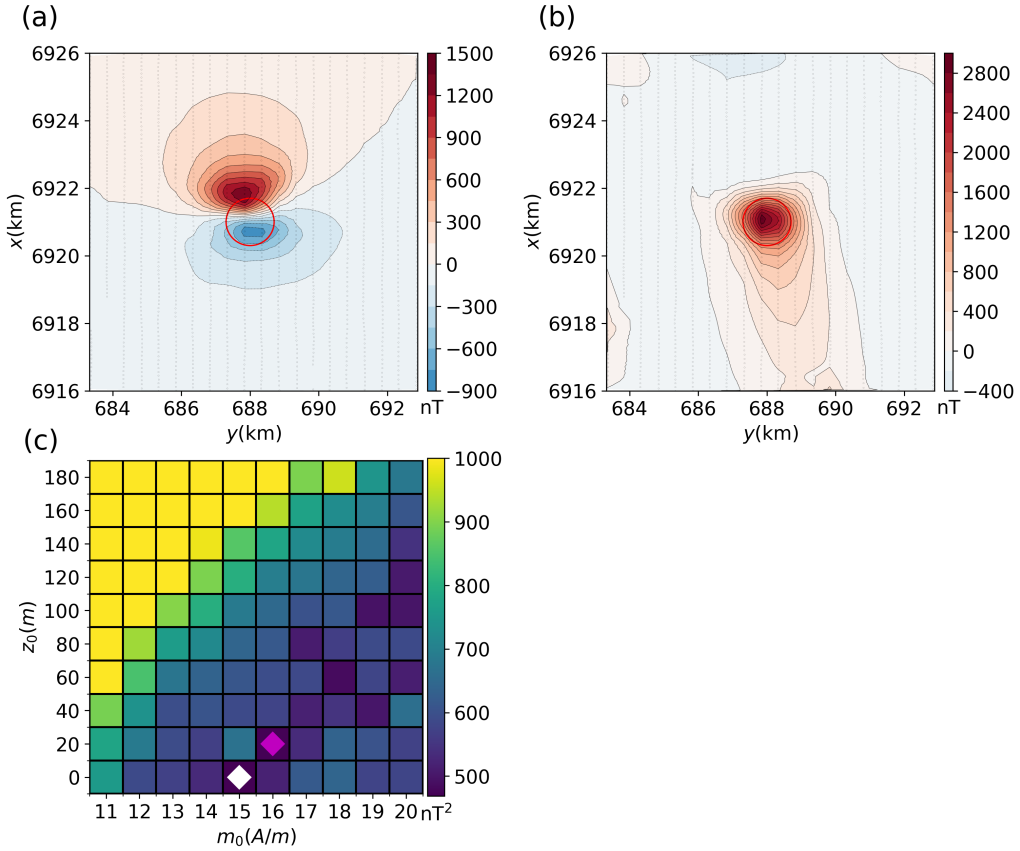


Figure 15. Application to field data over the Anitápolis complex, Brazil. (a) Residual total-field anomaly to be inverted over the area delimited by the magenta rectangle in Fig. 14. The red circle represents the horizontal projections of the initial approximation $\hat{\mathbf{p}}_{(0)}$. (b) RTP anomaly of the residual total-field anomaly shown in panel (a). (c) Discrete map of the goal function $\Gamma(\mathbf{p}, m_0, z_0)$ (Eq. 3) produced by the estimates $\hat{\mathbf{p}}_{(f)}$ obtained with a 6×6 grid of tentative values for depth to the top z_0 and total-magnetization intensity m_0 . The white and magenta diamonds pinpoint, respectively, two pairs of m_0 and z_0 whose goal functions are close to each other. The magenta diamond pinpoints the estimated model that produces the smallest value of $\Gamma(\hat{\mathbf{p}}_{(f)}, m_0, z_0)$. The white diamond pinpoints an alternative model whose depth to the top is $z_0 = 0$ indicating a possible outcropping not corroborated by the literature.

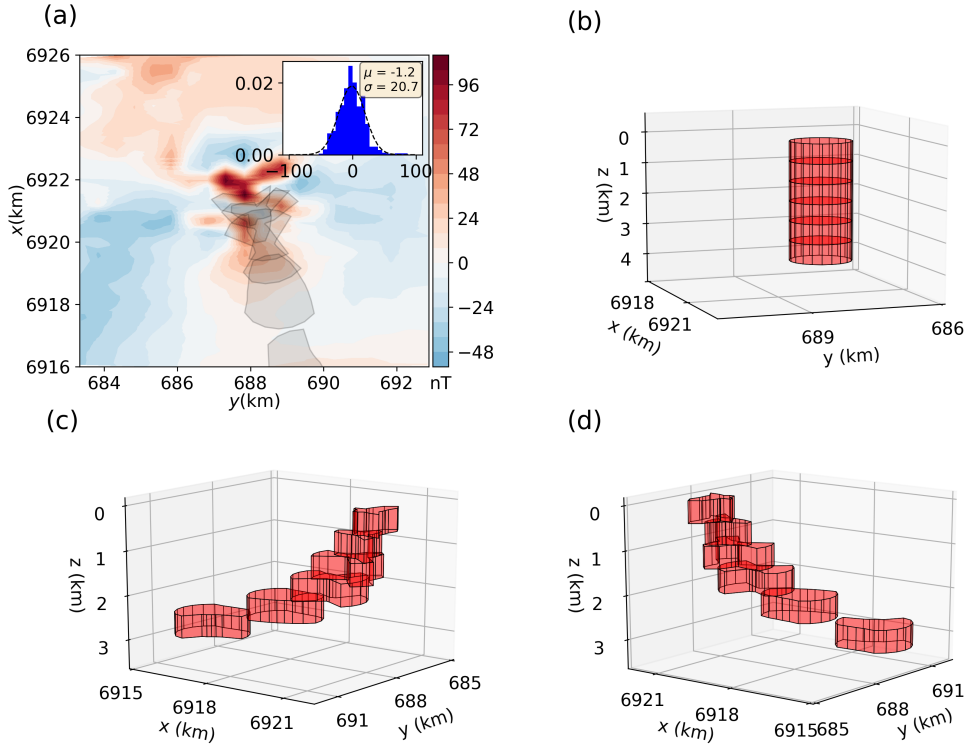


Figure 16. Application to the field data over the Anitápolis complex, Brazil. The non-outcropping estimated model producing the smallest goal function ($\Gamma(\hat{\mathbf{p}}_{(f)}, m_0, z_0)$, Eq. 3) represented by the magenta diamond in Fig. 15c. (a) Residuals between the observed data (Fig. 15a) and the predicted data (not shown) produced by the estimated model. The inset shows the histogram of the residuals and the fitted normal Gaussian curve (dashed line) with mean $\mu = -1.2$ nT and standard deviation $\sigma = 20.70$ nT. The light-gray polygons represent the horizontal projection of the estimated model onto the residual map. (b) Perspective view of the initial approximation (red prisms). (c) and (d) Perspective views of the estimated model (red prisms).

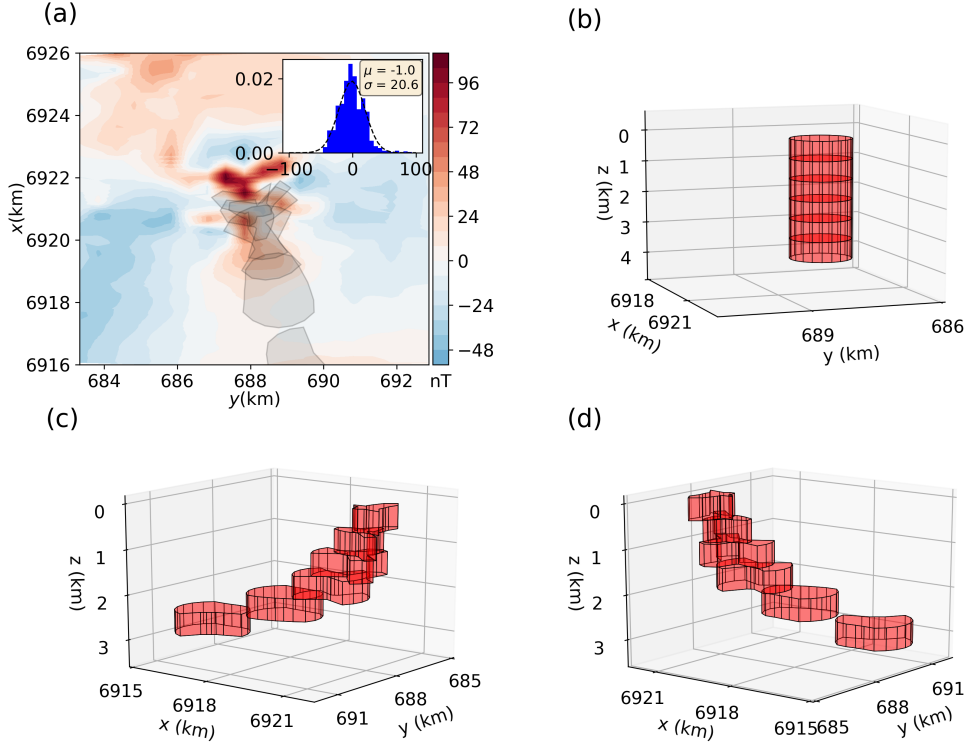


Figure 17. Application to the field data over the Anitápolis complex, Brazil. Outcropping estimated model represented by the white diamond in in Fig. 15c. (a) Residuals between the observed data (Fig. 15a and the predicted data (not shown) produced by the estimated model. The inset shows the histogram of the residuals and the fitted normal Gaussian curve (dashed line) with mean $\mu = 1.0$ and standard deviation $\sigma = 20.6$. The light-gray polygons represent the horizontal projection of the estimated model onto the residual map. (b) Perspective view of the initial approximation (red prisms). (c) and (d) Perspective views of the estimated model (red prisms).